Ultrashort Laser Pulses
and Applications

Edited by W. Kaiser

With Contributions by
D. H. Auston K. B. Eisenthal R. M. Hochstrasser
C. K. Johnson W. Kaiser A. Laubereau
D. von der Linde A. Seilmeier C. V. Shank W. Zinth

With 196 Figures

Sektion Physik der
Universität München
Viererbibliothek
8000 München 40
Schellingstraße 4/IV
VB 4867

Springer-Verlag Berlin Heidelberg New York
London Paris Tokyo

Professor Dr. Wolfgang Kaiser
Physik Department E11, Technische Universität, Arcisstr. 21
D-8000 München 2, Fed. Rep. of Germany

Managing Editor:
Dr. Helmut K. V. Lotsch
Springer-Verlag, Tiergartenstraße 17
D-6900 Heidelberg, Fed. Rep. of Germany

ISBN 3-540-18605-0 Springer-Verlag Berlin Heidelberg New York
ISBN 0-387-18605-0 Springer-Verlag New York Berlin Heidelberg

Library of Congress Cataloging-in-Publication Data. Ultrashort laser pulses and applications. (Topics in applied physics; v. 60) Includes bibliographies and index. 1. Laser pulses, Ultrashort. I. Kaiser, W. (Wolfgang), 1925– . II. Auston, D. H. III. Series. QC689.5.L37U469 1988 621.36′6 88-2009

This work is subject to copyright. All rights are reserved, whether the whole or part of the material is concerned, specifically the rights of translation, reprinting, reuse of illustrations, recitation, broadcasting, reproduction on microfilms or in other ways, and storage in data banks. Duplication of this publication or parts thereof is only permitted under the provisions of the German Copyright Law of September 9, 1965, in its version of June 24, 1985, and a copyright fee must always be paid. Violations fall under the prosecution act of the German Copyright Law.

© Springer-Verlag Berlin Heidelberg 1988
Printed in Germany

The use of registered names, trademarks, etc. in this publication does not imply, even in the absence of a specific statement, that such names are exempt from the relevant protective laws and regulations and therefore free for general use.

Typesetting: Asco Trade Typesetting Limited, Hong Kong
Printing and binding: Brühlsche Universitätsdruckerei, Giessen
2154/3150-543210

Contents

1. Introduction. By W. Kaiser 1
1.1 Organisation of the Book 2

2. Generation of Ultrashort Optical Pulses
By C. V. Shank (With 20 Figures) 5
2.1 Introduction 5
2.2 Mode-locking 5
  2.2.1 Basic Concepts 5
  2.2.2 Active Mode-locking 7
  2.2.3 Synchronous Pumping 8
  2.2.4 Passive Mode-locking 9
    a) Type 1: Giant-Pulse Lasers 10
    b) Type 2: Continuous Lasers 11
2.3 Short Pulse Laser Systems 13
  2.3.1 Dye Lasers 13
    a) Synchronous Mode-locking 13
    b) Passive Mode-locking 15
    c) Hybrid Mode-locking Techniques 18
    d) Amplification 19
  2.3.2 Color Center Lasers 22
  2.3.3 Novel Pulse Generation Techniques 23
  2.3.4 Diode Lasers 24
2.4 Pulse Compression 25
  2.4.1 Theory 26
  2.4.2 Compression Experiments 29
References 31

3. Optical Nonlinearities with Ultrashort Pulses
By A. Laubereau (With 27 Figures) 35
3.1 Nonlinear Polarization 35
3.2 Three-Wave Interactions 36
  3.2.1 Second Harmonic Generation 36
  3.2.2 Sum-Frequency Generation and Its Application for UV Pulses 42
  3.2.3 Difference-Frequency Generation and Down-Conversion to the Far Infrared 45

- 3.2.4 Stimulated Parametric Interaction 47
  - a) Stimulated Parametric Generators 49
  - b) Optical Parametric Amplifiers 50
  - c) Synchronously Coupled Parametric Oscillators . . 51
  - d) Stimulated Parametric Emission in Extended Spectral Regions 52
- 3.2.5 Further Applications 53
  - a) Second Harmonic Probing 53
  - b) Ultrafast Parametric Light Gates 54
  - c) Analysis of Pulse Shape 56
- 3.3 Four-Wave Interactions 60
  - 3.3.1 Sum-Frequency Generation 60
    - a) Third and Higher Order Harmonic Generation . . 60
    - b) Four-Wave Up-Conversion 62
  - 3.3.2 Four-Wave Difference-Frequency Mixing 63
    - a) General Discussion 64
    - b) Degenerate Four-Wave Mixing (DFWM) 66
  - 3.3.3 Stimulated Four-Wave Interactions 68
    - a) Stimulated Four-Wave Parametric Emission . . . 69
    - b) Optical Phase Conjugation 70
    - c) Stimulated Raman Scattering and Related Raman Interactions 73
  - 3.3.4 Further Four-Wave Interactions 83
    - a) Induced Population Gratings 83
    - b) The Coherence Peak 88
    - c) Continuum Generation 90
    - d) Ultrafast Bistability and Hysteresis 91
- 3.4 Short Pulse Nonlinearities with Special Boundary Conditions 94
  - 3.4.1 Nonlinear Effects at Interfaces 94
  - 3.4.2 Quantum Size Effects in Nonlinear Optics 97
  - 3.4.3 Nonlinear Pulse Propagation in Optical Fibers . . . 98
- 3.5 Conclusions 101
- References 102

4. Ultrashort Interactions in Solids
By D. von der Linde (With 42 Figures) 113
- 4.1 Exciton Dynamics 114
  - 4.1.1 Exciton-Polariton Dispersion 115
  - 4.1.2 Exciton Relaxation 119
  - 4.1.3 Exciton Screening 123
- 4.2 Electron-Hole Dynamics 129
  - 4.2.1 Electron-Hole Plasma 130
  - 4.2.2 Carrier Thermalization 137
  - 4.2.3 Electronic Relaxation in Disordered Materials and Quantum Wells 142

4.3 Phonon Dynamics 146
  4.3.1 Optical Phonon Lifetimes 149
  4.3.2 Relaxation of Incoherent Phonons 152
  4.3.3 Multiphonon States 156
4.4 Ultrafast Phase Transformations 159
  4.4.1 Amorphization 161
  4.4.2 Surface Melting 164
  4.4.3 Density of Electrons and Holes 169
  4.4.4 Electron and Lattice Temperature 172
4.5 Concluding Remarks 177
References 178

5. Ultrafast Optoelectronics. By D. H. Auston (With 26 Figures) . 183
5.1 Introduction 183
5.2 Optoelectronic Device Concepts 185
5.3 Materials for Ultrafast Optoelectronics 188
  5.3.1 Photoconducting Materials 188
    a) Intrinsic Speed of Response of Semiconductors . . 189
    b) High Electric Field Effects 191
    c) Trapping and Recombination 191
    d) Radiation Damage 192
    e) Carrier Mobilities 193
    f) Other Photoconducting Materials 194
  5.3.2 Electro-optic Materials 195
    a) Selection of Electro-optic Materials for Picosecond Optoelectronics 196
5.4 Generation and Detection of Ultrashort Electrical Pulses . 198
  5.4.1 Picosecond Photoconductors 198
    a) Response of an Ideal Photoconductor in a Transmission Line 200
    b) Photoconducting Electrical Pulse Generators . . . 200
    c) Photoconducting Electronic Sampling 202
    d) Electronic Autocorrelation Measurements 203
  5.4.2 Electro-optic Devices 204
    a) Electro-optic Sampling 204
    b) Optical Rectification 207
    c) Electro-optic Cherenkov Radiation 208
  5.4.3 Ultrafast Electrical Transmission Lines 209
5.5 Optoelectronic Measurement Systems and Their Applications 211
  5.5.1 Optoelectronic Measurement Systems 211
    a) Sensitivity 212
    b) Timing Accuracy 212
    c) Non-invasive Probing 212
    d) Low Temperature Environments 212

e) High Power 213
f) Simultaneous Time and Frequency Measurements. 213
g) Electrical Isolation 213
5.5.2 Characterization of High Speed Discrete Devices . . 214
a) Photoconductive Sampling of High Speed Photodetectors 214
b) Electro-optic Sampling of High Speed Photodetectors 214
c) Optical Mixing in Photodetectors 214
d) Impulse Response of High Speed Transistors . . . 215
e) Picosecond Photoemissive Sampling 217
5.5.3 Optoelectronic Measurements of Integrated Circuits . 217
a) Substrate Probing of GaAs Integrated Circuits . . 218
b) A Picosecond Electro-optic Wafer Prober 218
c) Charge Density Probing in Integrated Circuits . . 219
d) Direct Optical Stimulation of Integrated Circuits . 219
e) Integrated Photoconductors 220
5.5.4 Microwave, Millimeter-Wave, and Far-Infrared Applications 221
a) Photoconductive Switching and Gating 221
b) Optical Rectification 222
c) Phase Modulation of Microwave and Millimeter Waves 223
d) Radio Frequency Mixing 223
e) Photoconducting Antennas 224
5.5.5 High Power Optoelectronic Switches 226
a) Applications of High Power Photoconductors . . 227
5.6 Discussion 228
References 229

6. Ultrafast Coherent Spectroscopy
By W. Zinth and W. Kaiser (With 20 Figures) 235
6.1 Theory of Time-Resolved Coherent Spectroscopy 236
6.1.1 The Theoretical Model 236
6.1.2 Equations of Motion 237
6.1.3 Ultrafast Coherent Techniques 239
a) One Excitation Pulse 239
b) Two Excitation Pulses 240
c) Three Excitation Pulses 241
6.1.4 Electric Dipole and Raman-Type Transitions 241
a) Electric Dipole Transitions 241
b) Raman-Type Transitions 242
c) Pulse Area and Population Changes in Ultrafast Coherent Experiments 243

6.2 Coherent Spectroscopy Using a Single Excitation Process . 244
  6.2.1 Time-Resolved Coherent Raman Spectroscopy of a Single Homogeneously Broadened Transition 244
    a) Experimental Arrangements 246
    b) Dephasing in Liquids 247
    c) Vibrational Transitions in Solids 251
    d) The Collision Time 255
  6.2.2 Time-Resolved Coherent Raman Scattering of a Distribution of Resonance Frequencies 256
    a) Time-Domain Experiments 256
    b) Transient Frequency-Domain Experiments 259
  6.2.3 Resonant Pulse Propagation in the Infrared 262
6.3 Coherent Spectroscopy Using Multiple Excitation Processes 264
  6.3.1 Ultrafast Two-Pulse Echo Spectroscopy 265
  6.3.2 Three-Pulse Echos 267
    a) Measurements of Energy Relaxation Times . . . 269
    b) Measurements of Dephasing Times 270
    c) Accumulated Three-Pulse Echos 271
    d) Two-Color Echos 271
6.4 Summary 273
6.5 Appendix 273
References 274

7. Ultrashort Intramolecular and Intermolecular Vibrational Energy Transfer of Polyatomic Molecules in Liquids
By A. Seilmeier and W. Kaiser (With 22 Figures) 279
7.1 Experimental Techniques 280
  7.1.1 Excitation 280
  7.1.2 Probing 282
  7.1.3 Experimental System 284
7.2 Vibrational Population Lifetimes T_1 of Small Molecules in the Electronic Ground State S_0 285
  7.2.1 Experimental Data 286
  7.2.2 Theoretical Interpretation and Examples 290
    a) $CH_2=CCl_2$ 292
    b) *trans*-$CHCl=CHCl$ 293
7.3 Vibrational Redistribution in Large Molecules in the Ground State S_0 294
  7.3.1 The Redistribution Time 295
  7.3.2 The Vibrational Distribution 297
  7.3.3 The Concept of Internal Temperature 301
7.4 Intermolecular Transfer of Vibrational Energy of Large Molecules to the Surrounding Solvents 303
  7.4.1 Molecular Excitation with Infrared Pulses 304

7.4.2 Molecular Excitation via Rapid Internal Conversion . 305
7.4.3 Discussion and Model for Energy Transfer 306
7.5 Equalization of Energy in Liquids Measured with a Molecular Thermometer 309
7.5.1 The Molecular Thermometer 309
7.5.2 Energy Transfer Processes 310
7.5.3 Experimental Observations 311
7.6 Intramolecular Vibrational Relaxation of Large Molecules in the First Excited Electronic State S_1 314
References 315

8. Ultrafast Chemical Reactions in the Liquid State

By K. B. Eisenthal (With 16 Figures) 319
8.1 Introduction 319
8.2 Fast Chemical Reactions – Solvent Effects 319
8.3 Photoisomerization 320
8.3.1 Kramers Model of a Chemical Reaction 321
8.3.2 Photoisomerization at Low Densities 323
8.3.3 Photoisomerization of Polar Molecules 325
8.3.4 Photoisomerization with Femtosecond Pulses 327
8.4 Photodissociation and Recombination of Molecular Iodine in Solution 328
8.5 Chemical Intermediates 329
8.5.1 Role of Charge Transfer in Chemical Reactions . . . 329
a) Hydrogen Atom Transfer by Electron Plus Proton Transfer 330
b) Electron Donor–Acceptor Complexes 332
8.5.2 Carbenes 333
a) Spin Relaxation in Carbenes – Solvent and Structure Effects 334
b) Photochemistry of Chemical Intermediates 336
8.5.3 Nitrenes 337
8.5.4 Photofragmentation of Singlet Oxygen Precursors . . 338
8.5.5 Biradicals 339
8.6 Excited-State Proton Transfer 341
8.6.1 The Naphthols – Intermolecular Proton Transfer . . 342
8.6.2 Intramolecular Proton Transfer 343
a) Transfer in Non-Hydrogen-Bonding Solvents . . . 343
b) Transfer in Hydrogen-Bonding Solvents 345
c) Double Proton Transfer 348
8.7 Reactions in Bulbs and Beams 349
8.8 Concluding Remarks 350
References 350

9. Biological Processes Studied by Ultrafast Laser Techniques
By R. M. Hochstrasser and C. K. Johnson (With 23 Figures) . . 357
9.1 Heme Proteins 357
  9.1.1 Optical Spectroscopy of Heme Proteins 359
  9.1.2 Structural Information 363
  9.1.3 Transient Raman Spectroscopy 364
  9.1.4 Picosecond Transient Infrared Spectroscopy 367
  9.1.5 Protein Dynamics 367
  9.1.6 Fluorescence of Tryptophans in Mb and Hb 368
  9.1.7 Molecular Dynamics Simulations 372
  9.1.8 Geminate Recombination 374
  9.1.9 Photophysics of Hemes and Heme Proteins 375
  9.1.10 Laser Induced Heating 377
  9.1.11 Summary 380
9.2 Photosynthesis 380
  9.2.1 Electron Transfer 381
  9.2.2 Bacterial Reaction Centers 384
  9.2.3 Antenna Energy Transfer 390
  9.2.4 Reaction Centers in Green Plants 395
9.3 Rhodopsin and Bacteriorhodopsin 396
  9.3.1 Introduction and Background 396
  9.3.2 Rhodopsin and Bacteriorhodopsin Photochemistry . 396
  9.3.3 Picosecond Experiments 401
    a) Visual Pigments 401
    b) Purple Membrane Pigments 404
  9.3.4 Summary 409
References 409

Subject Index 419

6. Ultrafast Coherent Spectroscopy

Wolfgang Zinth and Wolfgang Kaiser

With 20 Figures

Coherent spectroscopy, initially started in the mid-sixties, is intimately conncected with the development of intense coherent light sources. The generation of ultrashort light pulses enabled coherent spectroscopy to be extended to real-time measurements of rapid dynamic processes on the time scale of 10^{-12} s. The early measurements of picosecond time-resolved coherent Raman scattering in 1971 were followed by numerous time-resolved techniques adapted to a variety of ultrafast phenomena. Most investigations are concerned with rapid dynamic processes in the condensed phases. The experimental progress stimulated theoretical investigations, improving our understanding of the interactions in liquids and solids. In recent years, a number of dynamic relaxation processes have been elucidated.

The title of this chapter, *Ultrafast Coherent Spectroscopy*, requires some explanation since it implies investigations in the time *and* frequency domain. Actually, it adequately characterizes the present situation. Coherent techniques give information on dynamic processes in the time domain as well as on linewidths and line positions in the frequency domain.

Numerous ultrafast investigations are concerned with coherent Raman scattering by molecular levels in the electronic ground state. The experimental techniques are well established on the picosecond time scale. Currently, these experiments are being extended to the study of even faster processes in the femtosecond time domain. A substantial fraction of coherent experiments deal with the study of vibrational levels in excited electronic states. Here, echo and induced-grating experiments have been successfully applied to reveal the relaxation dynamics.

The present chapter is organized as follows: In Sect. 6.6.1 the theoretical background of ultrafast coherent spectroscopy is given together with a short description of dynamical processes in condensed matter. Section 6.2 reports on time-resolved investigations using a single excitation process. Various time resolved coherent Raman and infrared techniques are discussed. Finally, in Sect. 6.3 echo-type experiments, i.e. experimental techniques with multiple excitation are presented.

6.1 Theory of Time-Resolved Coherent Spectroscopy

This section deals with the principles of time-resolved coherent experiments in a semi-classical approach. The electromagnetic light field is treated classically, the molecular system quantum-mechanically by its density matrix. Dynamic interaction processes between molecules have two important relaxation times – the phase relaxation time T_2 and the energy relaxation time T_1. We shall repeatedly refer to the relationship between time-domain coherent experiments and frequency-domain steady-state measurements.

6.1.1 The Theoretical Model

Coherent spectroscopy is presented here as a tool to investigate transitions between different energy levels or – more precisely – to study the transition frequencies and the relaxation processes related to these energy states. The essential features of the theoretical model are:

i) Of the many molecular transitions we treat only two levels, the ground state $|b\rangle$ and the excited state $|a\rangle$ separated by the energy $E = \hbar\omega_0$. All other states are assumed not to interact with the electromagnetic excitation and probing fields. This approach is well justified for most molecular systems [6.1].

ii) We assume that each molecular two-level system is only weakly interacting with the other molecules which are assumed to act as a fluctuating bath [6.2–6]. The Hamiltonian H of the molecule is written as a sum of an unperturbed Hamiltonian H_0 and two interaction Hamiltonians, the latter are: H_{im} which gives the interaction between the molecules and H_{ie} characterizing the interaction of the molecules with the electromagnetic fields [6.7,8]. The molecular interaction consists of a static contribution which leads to a constant frequency shift, and of a fluctuating contribution which modulates the resonance frequency and leads to a broadening of the transition band. The microscopic nature of the dynamic interaction may be understood in liquids in terms of "collisions" between individual molecules [6.2,4]. The collision process will be treated in detail in the context of Sect. 6.2.1. A major interaction in solids is caused by the thermal distribution of the acoustic phonons. In the macroscopic ensemble of two-level systems the dynamic interaction leads to relaxation time constants in the equation of motion (see below).

iii) The ensemble of two-level systems is described by the density matrix ρ with the diagonal elements ρ_{aa} and ρ_{bb} and the off-diagonal elements $\rho_{ab} = \rho_{ba}^*$. The density matrix follows the equation of motion

$$\frac{\partial \rho}{\partial t} = \frac{\mathrm{i}}{\hbar}[\rho, H] \ . \tag{6.1}$$

iv) The electromagnetic field is treated classically, since the number of photons is quite large in most coherent experiments. We work with plane waves, i.e.

the fields have the form: $E = E_0 \cos(\Omega t + kr)$ and consider electric dipole interactions with the Hamiltonian $H_{\mathrm{ie}} = \hat{\mu}E(t)$. $\hat{\mu}$ is the component of the dipole operator along the direction of the electric field E with $\mu_{aa} = \mu_{bb} = 0$ and $\mu_{ba} = \mu_{ab} = \mu$.

The evolution of the electromagnetic fields is described by the wave equation

$$\Delta E - \frac{n^2}{c^2}\frac{d^2 E}{dt^2} = \frac{1}{\varepsilon_0 c^2}\frac{d^2 P^{\mathrm{NL}}}{dt^2} \; . \tag{6.2}$$

The source term on the right-hand side of (6.2) describes the generation of light fields. The nonlinear polarization is proportional to the macroscopic dipole moment, $P = N\langle\hat{\mu}\rangle = N \times \mathrm{Tr}\{\hat{\mu}\rho\} = N\mu(\rho_{ab} + \rho_{ba})$, where N is the number of molecules per unit volume. Thus the radiation intensity observed in the coherent experiment is proportional to $|N\,\mathrm{Tr}\{\hat{\mu}\rho(t)\}|^2$.

6.1.2 Equations of Motion

Here we discuss the equations for the different components of the density matrix. The system of equations can be solved in a formal way by simple multiplication of matrices. In this way it is possible to readily see the salient features of the coherent spectroscopy. The discussion presented here follows a treatment given by *Hesselink* and *Wiersma* [6.9].

The equation of motion (6.1) is rewritten in (6.3–5) for the different density matrix elements. The electric field is coupled to the molecules via the interaction Hamiltonian $H_{\mathrm{ie}} = -\hat{\mu}E(t)$. It is convenient to introduce $\tilde{\rho}_{ba} = \rho_{ba}\exp(\mathrm{i}\Omega t)$ and to apply the rotating frame approximation.

$$\dot{\rho}_{aa} = \frac{\mathrm{i}\mu E_0}{2\hbar}(\tilde{\rho}_{ba}\mathrm{e}^{-\mathrm{i}kr} - \tilde{\rho}_{ab}\mathrm{e}^{\mathrm{i}kr}) - \frac{\rho_{aa}}{T_1} \; , \tag{6.3}$$

$$\dot{\tilde{\rho}}_{ba} = \frac{\mathrm{i}\mu E_0}{2\hbar}(\rho_{aa} - \rho_{bb})\mathrm{e}^{-\mathrm{i}kr} + \left(\mathrm{i}\Delta - \frac{1}{T_2}\right)\tilde{\rho}_{ba} \; , \tag{6.4}$$

$$\dot{\rho}_{bb} = 1 - \rho_{aa} \; . \tag{6.5}$$

Δ determines the detuning between the driving frequency Ω and the molecular resonance frequency ω_0, i.e. $\Delta = (\omega_0 - \Omega)$. It is assumed in (6.3–5) that the molecular system consists only of two levels $|a\rangle$ and $|b\rangle$. The equations may be modified to describe other situations, e.g. when relaxation to a third level is relevant. In the latter case one has to extend (6.5).

The significance of the relaxation times T_1 and T_2 is readily seen, when the electric field is turned off, i.e. for $E_0 = 0$. The energy relaxation time T_1 describes the relaxation of the population of level $|a\rangle$ with $\rho_{aa}(t) = \rho_{aa}(0)\exp(-t/T_1)$. The phase relaxation time T_2 determines the decay of the dipole moment $P = N\mu(\rho_{ba} + \rho_{ab})$ with $P(t) = P(0)\exp(-t/T_2)$. There are three contributions which determine the dephasing of the system. (i) The macroscopic dipole moment P

may decay by orientational motion of the individual molecules (orientational relaxation time T_R); (ii) the molecules may "get out of step", i.e. lose their phase relation by interaction with the surroundings (pure dephasing time T_2^*); (iii) the population of the upper level may decay (energy relaxation time T_1). The observed effective dephasing time T_2 is related to the individual time constants as follows: $1/T_2 = 1/T_R + 1/T_2^* + 1/(2T_1)$.

The applied electric field excites the system to the upper level $|a\rangle$ via (6.3) and generates a polarization via (6.4). For the following discussion it is important to introduce the pulse area $A = \int \mu E/\hbar \, dt$ [6.10]. The magnitude of A frequently determines whether a certain nonlinear coherent process occurs or not, e.g. whether a photon echo may be observed. When the applied electric field is strong and the pulse area is large, $A \gg 2\pi$, repeated excitation and de-excitation processes occur, causing the population ρ_{bb} to oscillate with the Rabi frequency $\chi = \mu E/\hbar$. In most of the following investigations with short pulses one has $A < 1$.

Analytical solutions of (6.3–5) can be found for two limiting conditions:

i) Without an applied electric field the density matrix evolves freely. Only the relaxation processes influence $\rho(t)$. The four components of the density matrix may be asigned to a vector $\boldsymbol{\rho}$, as listed in the Appendix [Eq. (6.20)]. The density matrix at time t is obtained by a linear transformation from the initial density matrix $\boldsymbol{\rho}(0)$:

$$\rho_j(t) = \sum_{k=1}^{4} Y_{jk}(t)\rho_k(0) \quad \text{or} \quad \boldsymbol{\rho}(t) = \underline{\boldsymbol{Y}}(t)\boldsymbol{\rho}(0) \; . \tag{6.6a}$$

The transformation matrix contains exponentials of t/T_2 and t/T_1. It is given explicitly in the Appendix [Eq. (6.21)].

ii) When a resonant electric field of pulse area A is applied, which is short compared to the relaxation times T_1 and T_2, the density matrix at the end of the pulse is calculated by a linear transformation $\underline{\boldsymbol{X}}(A)$,

$$\boldsymbol{\rho}(A) = \underline{\boldsymbol{X}}(A)\boldsymbol{\rho}(0) \; . \tag{6.6b}$$

The elements of the transformation matrix $\underline{\boldsymbol{X}}(A)$ depend on the pulse area and the wave vector of the electric field. They are given in the Appendix, [Eq. (6.22)]. The important aspects of many coherent experiments can be seen from the analytical solutions. Experimentally one has periods of short excitations with pulse areas A_i, $i = a, b, \ldots$ and free evolution periods of durations $t_1, t_2, \ldots$ At the time of observation, t, after the final excitation pulse with area A_f, the density matrix is calculated as a product of the individual excitation and evolution matrices $\underline{\boldsymbol{X}}(A_i)$, $\underline{\boldsymbol{Y}}(t_i)$:

$$\boldsymbol{\rho}(t) = \underline{\boldsymbol{Y}}(t)\underline{\boldsymbol{X}}(A_f) \ldots \underline{\boldsymbol{Y}}(t_2)\underline{\boldsymbol{X}}(A_b)\underline{\boldsymbol{Y}}(t_1)\underline{\boldsymbol{X}}(A_a)\boldsymbol{\rho}(0) \; . \tag{6.7}$$

Detailed examples for the solution of (6.7) are given below in Sect. 6.1.3. Here we refer briefly to the situation depicted in Fig. 6.1c, where three excitation fields are applied. The density matrix at time t is as follows:

$$\rho(t) = \underline{Y}(t)\underline{X}(A_c)\underline{Y}(t_2)\underline{X}(A_b)\underline{Y}(t_1)\underline{X}(A_a)\rho(0) \ .$$

The treatment given above in (6.6,7) is well justified when the applied light fields are separated in time and the radiating polarization of the sample is small at all times t_i. In the more general case reference is made to the literature cited in Sect. 6.3.2.

6.1.3 Ultrafast Coherent Techniques

A short overview of coherent spectroscopy is given here. Two types of molecular systems are treated: System I contains molecules with a single resonance frequency ω_0 (homogenous broadening), while System II shows a distribution of resonance frequencies $f(\omega_0)$ (inhomogeneous broadening).

a) One Excitation Pulse

In the most elementary coherent experiment one short laser pulse traverses the sample. After the excitation of the system by the pulse with area A_a and wave vector k_a radiation is emitted from the sample in the direction k_a. From (6.7) one derives the polarization $P(t)$ observed at the time t after the excitation pulse $P(t) = \mu N[\rho_{ab}(t) + \rho_{ba}(t)]$:

$$P(t) \propto \int d\omega\, f(\omega) \mathrm{e}^{-\mathrm{i}\omega t} \mathrm{e}^{-t/T_2} \sin(A_a) \mathrm{e}^{-\mathrm{i}k_a r} \ . \tag{6.8}$$

A schematic of the decay of $P(t)$ is shown in Fig. 6.1a. The generated polarization has an amplitude proportional to sin (A_a); it has the same wave vector as the exciting light pulse. For the molecular system I with $f(\omega) = \delta(\omega - \omega_0)$

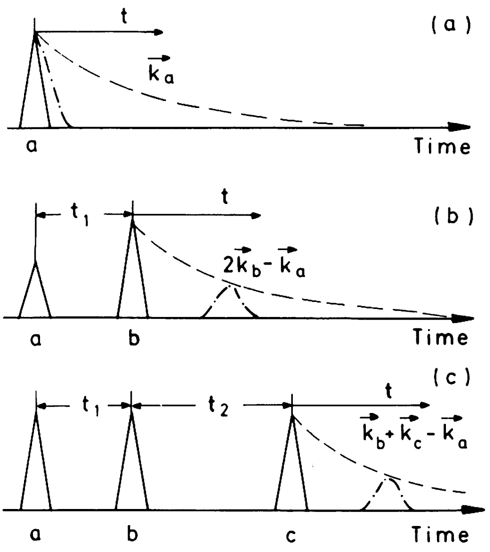

Fig. 6.1a–c. Schematic of various coherent techniques. The electric field pulses (*solid triangles*) excite the sample. The resulting coherent signal is shown for homogeneously broadened transitions (*dashed curves*), and for inhomogeneously broadened transitions (*dash-dotted curves*). (**a**) A single excitation pulse with wave vector k_a. Homogeneously broadened transitions lead to an exponential decay with dephasing time T_2, while inhomogeneous broadening induces a faster decay. (**b**) Two excitation pulses a and b with wave vectors $\boldsymbol{k}_a$ and $\boldsymbol{k}_b$ give echos in the direction $2\boldsymbol{k}_b - \boldsymbol{k}_a$. For inhomogeneously broadened transitions the echo is emitted at time $t = t_1$. The echo amplitude measured as a function of t_1 allows determination of the dephasing time T_2. (**c**) When three excitation pulses are used the coherent signal emitted in the direction $\boldsymbol{k}_b + \boldsymbol{k}_c - \boldsymbol{k}_a$ allows determination of the dephasing time T_2 and the energy relaxation time T_1

(broken line in Fig. 6.1a), the polarization decays exponentially with the dephasing time T_2. For a distribution of resonance frequencies $f(\omega_0)$ the decay of polarization starts exponentially, but accelerates due to the interference of the different resonance frequencies (dash-dotted line in Fig. 6.1a). With increasing width of the frequency distribution, the decay becomes more rapid and it is difficult – often impossible – to determine the dephasing time T_2. The explicit mathematical solution for the signal decay is readily obtained from (6.8). We note that the polarization is proportional to the product of the Fourier transform $g(t)$ of the distribution function $f(\omega_0)$ of the resonance frequencies times the exponential decay with $\exp(-t/T_2)$.

Investigations with single-pulse excitation are well established in ultrafast coherent spectroscopy. A series of interesting experiments are discussed in Sect. 6.2.

b) Two Excitation Pulses

When two excitation pulses of areas A_a and A_b separated by the evolution time t_1 (see Fig. 6.1b) are applied to the (molecular) system, a more complex time dependence of the coherent signal or of the density matrix is found. At time t after the second pulse, the radiating polarization consists of three contributions: two parts are independently produced by the two exciting pulses, radiating in the corresponding directions k_a and k_b. The two polarizations are described by (6.8). Of special interest is a third term, where the polarization evolves as follows:

$$P_{2\mathrm{PE}}(t) \propto \int \underline{d\omega\, f(\omega)\exp\Big[-\mathrm{i}\omega(t-t_1)} - \frac{t+t_1}{T_2}\Big] \times \sin A_a \sin^2\frac{A_b}{2}\exp[-\mathrm{i}(2k_b-k_a)r] \ . \tag{6.9}$$

The signal is emitted with the wave vector $2k_b - k_a$ and may readily be separated from the exciting beams. For a homogeneously broadened transition (System I), the peak of the polarization is proportional to $\exp(-t_1/T_2)$. The polarization decays at later times with $\exp(t/T_2)$ (see Fig. 6.1b, broken line). Quite different is the situation for strong inhomogeneous broadening (System II). Now the (underlined) interference term in (6.9) is removed at one delay time, $t = t_1$, and a delayed signal appears, i.e. one finds a photon echo with an amplitude proportional to $\exp(-2t_1/T_2)$ [6.11–13]. Variation of t_1, i.e. of the distance between the two exciting pulses, therefore enables one to deduce the dephasing time T_2 even for inhomogeneously broadened transitions [6.13]. (For the intermediate case with small inhomogeneous broadening see [6.14]).

An important aspect for the application of the photon echo technique is the dependence of the signal on the area of the excitation pulses. Good echo signals are generated for $A_a \simeq \pi/2$ and $A_b \simeq \pi$. For small areas A_a, $A_b \ll \pi$ the signal amplitude drops with $A_a A_b^2$ or the signal intensity with $(A_a A_b^2)^2$. We recall that in the case of a single excitation pulse the emitted signal intensity is proportional to A_a^2. Consequently, coherent echo experiments become more difficult when the transitions are weak and the pulses and relaxation times are very short.

c) Three Excitation Pulses

When three excitation pulses with areas A_a, A_b, and A_c separated in time by t_1 and t_2 are applied to the molecular system, a variety of coherent signals is produced: single excitation signals, two-pulse echos from each pair of the three pulses, and so-called three-pulse echos at the time $t = t_1$ after the third pulse, the latter echos are emitted in the direction $k_b + k_c - k_a$ (see Fig. 6.1c). The introduction of the third pulse allows one to measure the dephasing time T_2 of the molecular transition *and* to determine the energy relaxation time T_1. The application of three pulses gives considerable flexibility to the design of experiments. Similar limitations regarding the signal strength exist as in two-pulse experiments; the three-pulse echo intensities are proportional to $(\sin A_a \sin A_b \sin A_c)^2$. For small area pulse the echo signal decreases proportion to $A_1^2 A_2^2 A_3^2$. Experiments with ultrafast three-pulse echos have been performed for a number of electronic transitions. These are discussed in Sect. 6.3.2.

6.1.4 Electric Dipole and Raman-Type Transitions

The interaction between the system of interest and the light field depends on the specific type of interaction Hamiltonian H_{ie}. We address here two situations, the electric dipole and the Raman-type transitions. The common aspect of the (molecular) excitation is best demonstrated by introducing the operator $\hat{q}$ for the excitation coordinate (of the molecules). In the case of a vibrational transition, $\hat{q}$ represents the coordinate of the nuclear motion of the vibrating molecules. For an electronic transition, $\hat{q}$ is related to the motion of the electrons. For an ensemble of two-level systems the expectation value $\langle \hat{q} \rangle$, called the coherent or collective amplitude, is given by:

$$\langle \hat{q} \rangle = \mathrm{Tr}\{\rho \hat{q}\} = q(\rho_{ab} + \rho_{ba}) \ , \tag{6.10}$$

where $q_{ab} = q = \langle a | \hat{q} | b \rangle$ is the transition matrix element.

a) Electric Dipole Transitions

Electric dipole transitions are commonly investigated with light frequencies close to a resonance frequency. In this case the interaction cross sections are large and the polarizations resulting from the excitation process generate new electromagnetic waves.

The electric dipole moment $\boldsymbol{\mu}$ related to the transition between the levels $|a\rangle$ and $|b\rangle$ (of one molecule) is a vector; its direction (unit vector $\boldsymbol{u}$) is fixed in the reference frame of the molecule and its amplitude is proportional to the amplitude of the coordinate q: $\boldsymbol{\mu} = \boldsymbol{u}\, d\mu/dq\, q$[6.15,16]. The interaction of the dipole moment with an electric field is given by the Hamiltonian $H_{ie} = -\boldsymbol{\mu E} = d\mu/dq\, qE \cos\theta$, where θ is the angle between the dipole moment and the electric field. For an ensemble of molecules the relaxation of the total dipole moment $\langle \boldsymbol{\mu} \rangle$ as a function of time depends on (i) the orientational relaxation of the vector $\boldsymbol{u}$ (irrelevant in most solids) and (ii) the relaxation of the absolute value of the coherent amplitude $\langle \hat{q} \rangle$. This topic is the subject of intensive investigations discussed in this chapter.

It is of interest to compare the quantities measured in time-resolved coherent investigations and in steady-state spontaneous spectroscopy, i.e. the time dependence of the expectation values $\langle \hat{q} \rangle$ or $\langle \boldsymbol{\mu} \rangle$ with the absorption spectra [6.3,15]. The latter can be calculated from (6.3–5), when the left-hand side of the equations, i.e. the time-dependent terms, are equal to zero. One readily finds the absorption line to be of Lorentzian shape with a peak absorption cross section $\sigma = (d\mu/dq)^2 \omega T_2/(\varepsilon_0 cn\hbar)$ and a linewidth (FWHM) of $\Delta\nu = 1/\pi T_2$. Here ε_0 is the permittivity, n the refractive index, c the velocity of light, and $\hbar$ Planck's constant.

The absorption spectrum $J(\omega)$ may be related to the time-dependent dipole moment in a general way without referring to the special model introduced above. Line-shape theory gives [6.2–6,15,16]:

$$J(\omega) \propto \int_{-\infty}^{+\infty} \mathrm{e}^{\mathrm{i}\omega t} \phi(t)\, dt = \int_{-\infty}^{+\infty} \mathrm{e}^{\mathrm{i}\omega t} \langle\langle \mu(t)\mu(0) \rangle\rangle\, dt \;, \tag{6.11}$$

where $\langle\langle \cdots \rangle\rangle$ denotes the equilibrium ensemble average. According to (6.11) the spectral line shape is the Fourier transform of the correlation function $\phi(t)$, i.e. of the time dependence of $\mu(t)$, which is measured in straightforward coherent experiments [see Sect. 6.1.3(a)]. Introducing an exponential decay with time constant T_2 for the dipole moment in (6.11) one obtains the same Lorentzian line shape as determined above directly from (6.3–5).

b) Raman-Type Transitions

Raman type transitions have the advantage that excitation is possible with a wide range of available electromagnetic fields, i.e. resonance frequencies are not required. On the other hand, the Raman interaction is a weak, second-order process; the pulse area and the degree of excitation are small. In spite of this difficulty, ultrafast Raman spectroscopy has provided valuable new information. Direct observation of several rapid dynamic processes has become possible and superior spectral resolution was demonstrated in congested spectral regions.

According to *Placzek* [6.17], the interaction between a given vibrational mode and the electric field can be described by the interaction Hamiltonian $H_{\mathrm{ie}} = (\partial\underline{\alpha}/\partial q) q\boldsymbol{EE}/2$, where $d\underline{\alpha}/dq$ stands for the change of the electric polarizability tensor with the vibrational coordinate q. It leads to the excitation of the molecular mode (frequency ω_0) under the action of the light field E, provided that components i, j of the electric field exist, where the product $E_i E_j^*$ oscillates at the frequency ω_0. The Raman process may again be described by (6.3–5), if we replace the quantity μE_0 by $(\partial \underline{\alpha}/\partial q) q_{ab} E_i E_j/2$. In a similar way, the radiating polarization is obtained as

$$P_i = N\mu_i = N\frac{\partial \alpha_{ij}}{\partial q} E_j \langle \hat{q} \rangle \ . \tag{6.12}$$

The polarization is proportional to the electric field $\boldsymbol{E}$, i.e. the molecular excitation $\langle q \rangle$ leads to a scattered light field when monitored by a probing field. Without a probing field the coherent amplitude $\langle \hat{q} \rangle$ does not produce electromagnetic radiation. When the transition is electric dipole and Raman active, some light emission may occur, provided the molecules are in a crystal without inversion symmetry. This case will not be treated here. For isotropic Raman transitions the tensor $\partial \underline{\alpha}/\partial q$ is reduced to a scalar quantity $\partial \alpha/\partial q$. In this case, rotational motion of the molecules does not effect the evolution of the coherent signal and the decay of the coherent amplitude $\langle q \rangle$. The more complex case of an anisotropic Raman tensor has been treated in the literature by *Laubereau* and *Kaiser* [6.7], by *Kohles* and *Laubereau* [6.18], and by *Dick* [6.19]; it will not be discussed here in detail.

Comparing time-resolved coherent and spontaneous Raman scattering, one obtains very similar equations as in the case of electric dipole transitions. The spontaneous Raman line shape can again be calculated from (6.3–5) or from the line-shape theory [6.2–6]. The spectral shape is the Fourier transform of a molecular correlation function; for isotropic Raman lines it is proportional to the Fourier transform of $\langle\langle q(t) q(0) \rangle\rangle$.

c) Pulse Area and Population Changes in Ultrafast Coherent Experiments

For practical experiments it is important to know how strongly the (molecular) system is excited under the action of a light pulse. The strength of the excitation determines which type of coherent experiment can be performed with given light pulses. The important quantity is the pulse area A which is directly related to the changes of the population of the various levels [see (6.6,22)]; e.g. for a system initially in the ground state a short pulse with area A changes the ground-state population by $\Delta \rho_{bb} = (1 - \cos A)/2$. Using an exciting pulse with peak intensity I, duration t_p, and absorption cross section σ one estimates the pulse area to be $A = \mu E_0 t_p/\hbar = (2n^2 I T_2 \sigma/\hbar\omega_0)^{1/2}$. We assume here that the duration of the pulses is equal to the dephasing time. We now give numbers for the pulse area for three relevant examples using the following parameters: dephasing time $T_2 = 10^{-12}$ s, intensity $I = 10^{10}$ W/cm^2, refractive index $n = 1.5$.

i) For an infrared-active vibrational CH-stretching mode at $\lambda = 3\,\mu$m with $\sigma = 10^{-19}$ cm^2 one obtains $A = 2.6 \times 10^{-1}$ and $\Delta \rho_{bb} = 1.6 \times 10^{-2}$.

ii) For an electronic transition at $\lambda = 0.5\,\mu$m with $\sigma = 10^{-16}$ cm^2 one calculates $A = 3.4$ or $\Delta \rho_{bb} = 0.99$. The two examples show that electronic transitions may lead to large pulse areas making coherent experiments quite easy, while for vibrational transitions the observation of two- and three-pulse echos with echo amplitudes proportional to A^6 is difficult.

iii) For Raman active transitions the pulse area $A = 1/2(\partial\alpha/\partial q)q_{ab}t_{\mathrm{p}}E^2/\hbar$ may be calculated using the definitions of $\partial\alpha/\partial q$ and q_{ab} from the literature [6.8]. One obtains $A = In\lambda^2 t_{\mathrm{p}}\sqrt{\delta\sigma}/(\pi c\hbar)$, where $\delta\sigma$ is the Raman cross section integrated over one Steradian. Taking $\delta\sigma = 2.5 \times 10^{-29}$ from benzene [6.10] (which has a rather large Raman cross section for a molecular vibration) and $\lambda = 0.5\,\mu\mathrm{m}$ we compute an area A of $A = 1.9 \times 10^{-2}$ or a population change $\Delta\rho_{bb} \simeq 10^{-4}$. These numbers are even smaller than the values calculated for resonant infrared absorption, see (i). It is evident that under the present conditions, ultrafast Raman-echo experiments appear to be unrealistic, while single-pulse coherent Raman experiments are readily possible. It should be noted that considerably higher cross sections are found for resonant Raman transitions. Only under these conditions might ultrafast Raman-echo experiments become possible.

In this section a set of equations was introduced which allows one to treat time-resolved coherent spectroscopy within the framework of the model presented in Sect. 6.1.1. We have briefly outlined and compared different experimental methods for which applications are discussed in the following sections.

6.2 Coherent Spectroscopy Using a Single Excitation Process

We focus here on investigations of time-resolved coherent spectroscopy using single excitation processes. It is the aim of this section to demonstrate the different time-resolved techniques and to show the advantages of coherent techniques over spontaneous frequency-domain methods.

6.2.1 Time-Resolved Coherent Raman Spectroscopy of a Single Homogeneously Broadened Transition

The experiments of time-resolved coherent Raman spectroscopy are performed in two steps. First, the sample is excited by a pair of light pulses via transient stimulated Raman scattering (see Fig. 6.2, upper part) [6.20–23]. Subsequently, the degree of excitation is interrogated by a probe pulse, which is delayed in time relative to the excitation pulses. The probe pulse monitors the coherent amplitude by Raman scattering [6.1,7,8]. The experiments are described by two different sets of equations: the material equation governing the generation of the excitation under the action of the light fields [see (6.3–5)] and the wave equation (6.2) determining the light field due to the interaction with the material excitation. We recall that in coherent Raman processes the pulse areas are quite small [see Sect. 6.1.4(c)]. For this reason the changes of the diagonal elements of the density matrix are small and the off-diagonal elements may be calculated by using only

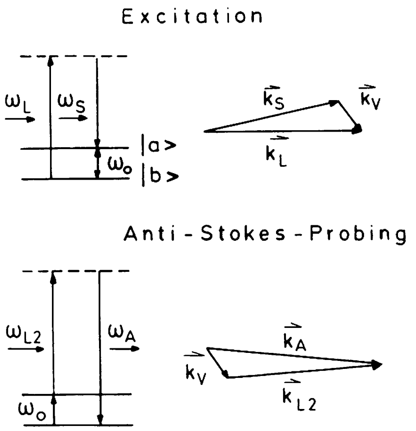

Fig. 6.2. Schematic of a time-resolved coherent Raman experiment. The excitation of the upper level $|a\rangle$ is accomplished via stimulated Raman scattering by the laser and Stokes pulses at frequencies ω_L and ω_s, respectively. The wave vectors of the two laser fields determine the wave vector of the coherent excitation, $\boldsymbol{k}_v = \boldsymbol{k}_L - \boldsymbol{k}_s$ (*upper part*). At a later time the coherent Raman probing process (*lower part*) with a second laser pulse E_{L2} ($\omega_{L2}, \boldsymbol{k}_{L2}$) monitors the coherent excitation. The coherent anti-Stokes signal emitted under phase matching conditions $\boldsymbol{k}_a = \boldsymbol{k}_{L2} - \boldsymbol{k}_v$ is a measure of the coherent amplitude at the probing time

(6.4). For Raman-type interactions (6.4) may be solved by direct integration. The electric field producing excitation consists of two components:

$$E = E_L \cos(-\omega_L t + k_L x) + E_s \cos(-\omega_s t + k_s x) \ ,$$

and for the coherent material excitation one makes the ansatz of a plane wave

$$\langle q \rangle = \frac{i}{2} Q \exp(-i\omega_0 t + k_v x) + \text{c.c.} = q_{ab}(\rho_{ab} + \rho_{ba}) \ .$$

With these expressions (6.4) yields the amplitude Q after one integration [6.1,7,8,24]:

$$Q(x,t) = \frac{i q_{ab}^2}{2\hbar} \frac{\partial \alpha}{\partial q} \int\limits_{-\infty}^{t} E_L(t',x) E_s^*(t',x) \exp\left[\frac{1}{T_2}(t'-t) + i\Delta t'\right] dt' \ . \qquad (6.13)$$

The excitation process is shown schematically in Fig. 6.2, upper part. The two components of the electric field at frequency ω_L and ω_s drive the vibration with frequency $\Omega = \omega_L - \omega_s$ close to the resonance frequency ω_0. The wave vector of the coherent amplitude k_v is determined by $k_v = k_L - k_s$. Q shows the properties discussed previously: a rapid rise with the driving force $E_L E_s^*$ and an exponential decay with $\exp(-t/T_2)$ of the freely vibrating system. The 'back' reaction of the coherent amplitude on the light fields is governed by the polarization $\boldsymbol{P}$:

$$\boldsymbol{P} = N \frac{\partial \alpha}{\partial q} \langle q \rangle \boldsymbol{E} + \underline{\chi}_{\text{NR}}^{(3)} \varepsilon_0 \boldsymbol{EEE} \ . \qquad (6.14)$$

The coupling of the wave equation and the material equation via the polarization leads to stimulated Raman scattering or Stokes/anti-Stokes coupling, which have been discussed in detail elsewhere [6.8,20–23,25–28]. The nonresonant nonlinear polarization $\chi^{(3)}_{\underline{\mathrm{NR}}}$ is due to distant electronic transitions. It leads to self-phase-modulation and nonresonant scattering [6.10,28].

For time-resolved coherent Raman spectroscopy a probing pulse is necessary to obtain information on the time dependence of the coherent amplitude (see Fig. 6.2, lower part). The third light pulse $E_{L2} = E_{L2}(t)\cos(-\omega_{L2}t + k_{L2}x)$ generates a radiative polarization according to (6.14). A short probing pulse at variable time delay t_D after the excitation pulses allows one to map out the time dependence of the coherent amplitude. The scattered signal at the anti-Stokes frequency $\omega_A = \omega_{L2} + \omega_0$ or at the Stokes frequency $\omega_{s2} = \omega_{L2} - \omega_0$ is observed. Efficient generation of the coherent signal requires phase matching, i.e. the wave vectors of the material excitation $\boldsymbol{k}_v$, the probing field $\boldsymbol{k}_{L2}$, and generated light, e.g. $\boldsymbol{k}_A$, have to satisfy the condition $\boldsymbol{k}_v + \boldsymbol{k}_{L2} = \boldsymbol{k}_A$.

a) Experimental Arrangements

A typical experimental system is depicted schematically in Fig. 6.3. A pumping laser source generates exciting and probing light fields at the frequencies ω_L, ω_s, and ω_{L2} in several frequency converters. In early experiments a simple optical system was used: the Stokes pulse was generated via stimulated Raman scattering of the strong laser pulse in the sample itself [6.29,30]. More recently, frequency conversion by dye lasers produced tunable Stokes pulses [6.31–34]. The exciting

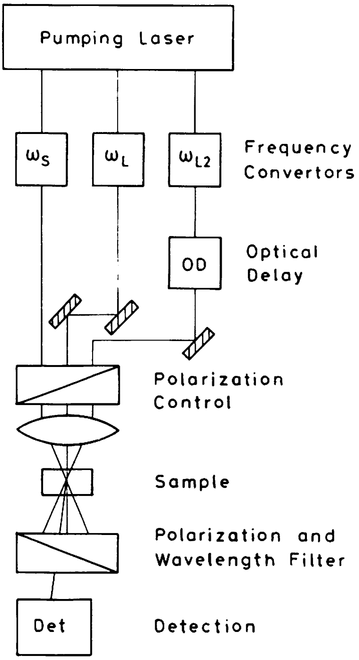

Fig. 6.3. Experimental system used for time-resolved coherent Raman scattering. Synchronized pulses at frequencies ω_L, ω_s, and ω_{L2} are generated by different frequency converters from one pumping laser source. The pulses at ω_L and ω_s excite the sample via stimulated Raman scattering. The coherent excitation is monitored by the delayed (optical delay OD) probing pulses at frequency ω_{L2}. The different beams cross in the sample at phase-matching angles. Polarization and wavelength filters separate the coherent signal from the excitation light

Stokes and laser pulses are focused at a specific angle into the sample generating the coherent material excitation. The probing light pulse at frequency ω_{L2} is delayed relative to the excitation process in the optical delay system OD and monitors the excited volume of the sample. The geometry of the exciting and probing beams in the sample have to be adjusted to obtain phase matching for the coherent probe-scattering process. In most experiments the signal intensities are much smaller than the intensities of the excitation pulses. Consequently, the coherently scattered light must be separated carefully from the incoming light beams by diaphragms and spectral and/or polarization filtering. The detection system is a highly sensitive photo-detector. Frequently, the spectra of the coherently scattered light are analyzed with the help of a spectrograph.

b) Dephasing in Liquids

A straightforward application of time-resolved coherent Raman spectroscopy on the picosecond time scale is the investigation of single Raman active vibrational transitions. Such an experiment was performed for the first time by *von der Linde* et al. [6.29] in 1971. The authors observed the coherent anti-Stokes signal for ethanol (C_2H_5OH) and carbontetrachloride (CCl_4) on the picosecond time scale.

A large number of other molecules and transitions have been studied in the meantime [6.32–43]. The state of the art of coherent measurements with high time resolution is demonstrated in two recent publications by *Gale* et al. [6.42] and by *Zinth* et al. [6.44]. In the first experiment, a Nd : glass laser system supplied light pulses with relatively long duration ($t_p = 5$ ps). The high time resolution was achieved by a specially designed excitation and probing system that allows the signal decay to be measured over 9 orders of magnitude. With the nearly Gaussian-shaped pulses from the Nd:glass laser, the decay of the response function (see broken curve in Fig. 6.4) accelerates with decreasing signal at later delay times. As a consequence, the favorably high signal-to-noise ratio of the experiment allowed the measurement of decay times considerably shorter than the pulse duration. In Fig. 6.4a the solid curve corresponding to the ν_1 mode of acetonitrile at $\nu/c = 2943\,\mathrm{cm}^{-1}$ shows an exponential decay over the entire observation range. This fact clearly demonstrates that the vibrational transition is homogeneously broadened with a dephasing time $T_2 = 1.63 \pm 0.07$ ps.

Superior time resolution is achieved with very short light pulses. *Zinth* et al. [6.44] introduced an experimental system with femtosecond pulses ($t_p \simeq 80$ fs) from a ring dye laser. A recent result is presented in Figs. 6.4b and 6.5. In Fig. 6.4b the same acetonitrile mode was studied as in Fig. 6.4a. Using femtosecond pulses the coherent signal is well separated from the autocorrelation trace, just 100 fs after time zero. Consequently, the decay time is determined with very high precision to be $T_2 = 1.70 \pm 0.02$ ps. In Fig. 6.5a and b the coherent signal decays are shown for the ν_2 and ν_7 modes of liquid acetone. In both cases one finds for delay times larger than 200 fs a clear exponential decay. The time constants are 510 ± 30 fs (ν_7 mode) and 305 ± 10 fs (ν_2 mode); i.e. one obtains

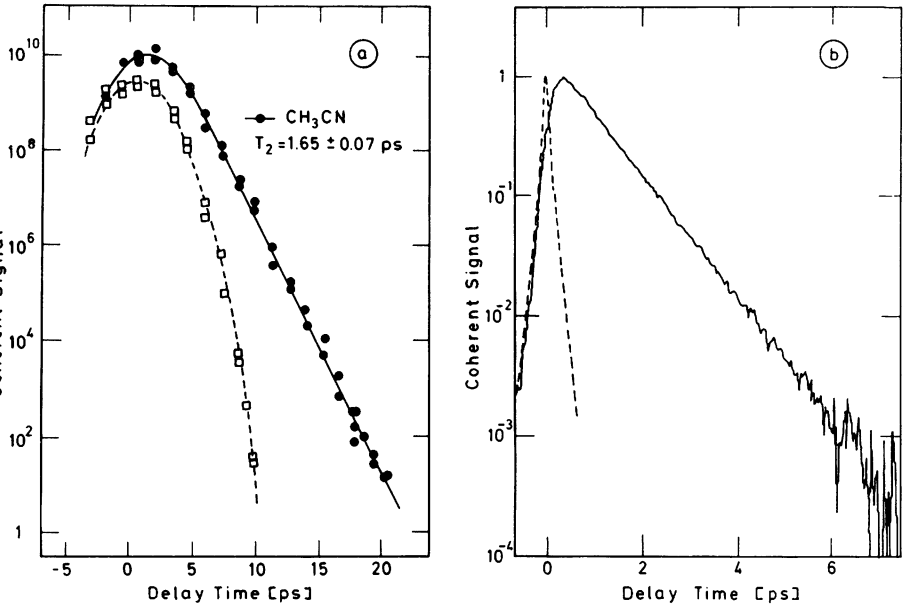

Fig. 6.4a, b. Coherent anti-Stokes signal for the ν_1 mode of acetonitrile plotted as a function of the time delay of the probing pulses. (**a**) Laser pulses of 5 ps duration were used. The signal is recorded over nine orders of magnitude. ●: Coherent response of acetonitrile CH_3CN. From the exponential decay a dephasing time $T_2 = 1.65 \pm 0.07$ ps is determined. o: Response function of the experimental system measured by coherent scattering in C_2H_5OH. (Redrawn from *Gale* et al. [6.42]). (**b**) Laser pulses of 80 fs duration were used. A ready separation between coherent signal and autocorrelation trace starts within 100 fs. The dephasing time is determined to be $T_2 = 1.70 \pm 0.02$ ps [6.44b]

dephasing times of $T_2 = 1020 \pm 60$ fs and 610 ± 20 fs. At shorter delay times the signal deviates from the pure exponential decay. In Fig. 6.5a this effect is mainly due to the nonresonant susceptibility. There may also be some residual influence from collisional processes (see below) which are not included in (6.3–5).

The experiments on time-resolved coherent Raman scattering have initiated a number of theoretical investigations treating dephasing and energy relaxation of vibrational levels in molecular liquids. *Fischer* and *Laubereau* [6.2] have estimated relaxation times assuming a binary collision between the molecules with exponential intermolecular interaction potential. Despite its several simplifying assumptions this model is capable of predicting dephasing times in liquids over a range of parameters such as temperature, concentration, and viscosity. A number of other theoretical approaches, e.g. molecular dynamics simulations, correlation function modelling, or hydrodynamic models have been discussed in the literature [6.45–60]. For a review see *Oxtoby* [6.3].

In many coherent experiments the initial signal is strongly affected by the nonresonant susceptibility $\chi_{NR}^{(3)}$ deviating substantially from the single exponential decay discussed theoretically (for an example see Fig. 6.5 or 6.6). The influence

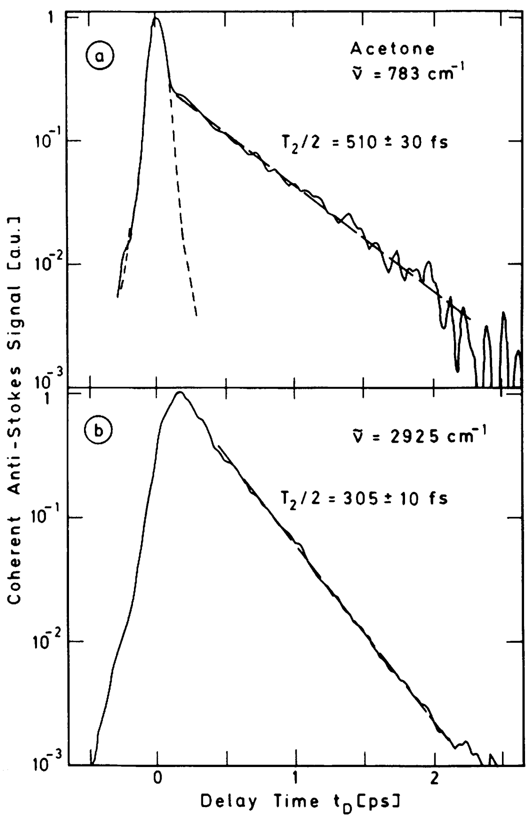

Fig. 6.5a, b. Coherent signal from aceton measured with femtosecond laser pulses. The ν_7 (**a**) and ν_2 (**b**) modes are studied. Exponential decay with time constants $T_2/2 = 510 \pm 30$ fs (ν_7) and 305 ± 10 fs (ν_2) are found at later delay times. The signal shape in (**a**) around time zero is influenced by the nonresonant susceptibility $\chi_{NR}^{(3)}$. The dashed curve shows the response function of the experiment measured with the help of sum-frequency generation in a nonlinear KDP crystal. The narrow response function clearly demonstrates the power of the experimental system to measure very short decay times [6.44]

of the nonresonant susceptibility $\chi_{NR}^{(3)}$ on time-domain coherent Raman experiments was investigated for the first time by *Zinth* et al. [6.61] in mixtures, where molecular modes of highly diluted molecules were studied. Figure 6.6 shows the data for the ν_1 mode of liquid CCl_4 (9 vol.%) dissolved in cyclohexane, C_6H_{12}, (experimental system Nd:glass laser with $t_p = 7$ ps). The peak of the scattered Stokes signal is close to $t_D = 0$, where the driving force ($E_L E_s^*$) overlaps with the probing light pulse. At first the signal decays very rapidly by a factor of 50; it subsequently decays more slowly with a time constant of $T_2/2 = 3.6$ ps (broken line). This time dependence is readily understood by taking into account the nonresonant susceptibility $\chi_{NR}^{(3)}$ of the system [see (6.14)]. The nonresonant susceptibility induces an additional signal close to time zero due to a polarization proportional to $\chi_{NR}^{(3)} E_L E_s E_{L2}$. This part of the signal has the time dependence of the experimental response function. At later delay times, the slower decay due to the resonantly excited solute molecules (CCl_4) takes over and determines the decay curve. Under the existing experimental conditions the later decay is close to an exponential (further details are given together with the discussion of results on pure CCl_4 in Sect. 6.2.2). Comparing the experimental signal curves with the

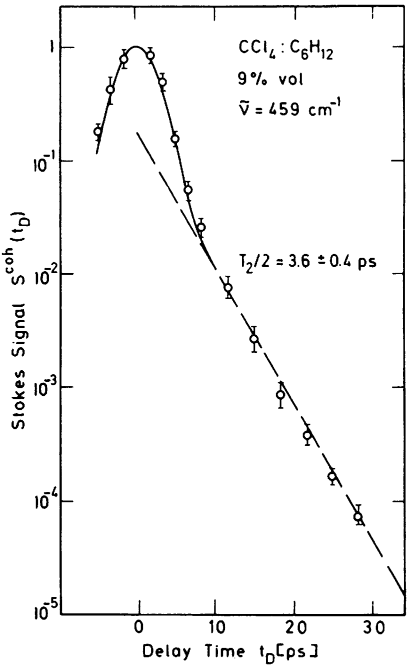

Fig. 6.6. Coherent signal from a mixture of CCl_4 and C_6H_{12}. Here, the effect of the nonresonant susceptibility $\chi_{NR}^{(3)}$ in a time resolved Raman experiments was demonstrated for the first time. While the exponential decay at later delay times is due to the resonant coherent excitation of the CCl_4 molecules, the signal peak at time zero originates from the nonresonant susceptibility $\chi_{NR}^{(3)}$ of the solvent molecules C_6H_{12} [6.61]

theory of (6.3–5) and (6.13,14) allows one to deduce the ratio of the nonresonant to the resonant susceptibility in the mixture.

The experimental results show that the resonant and the nonresonant part of the nonlinear susceptibility may be separated in a time-domain experiment. While at time zero, both the nonresonant and the resonant part contribute to the signal, the measurement at later delay time gives access to the resonant part of the susceptibility. This separation allows frequency-domain coherent anti-Stokes Raman experiments (CARS) without the disturbing influences of $\chi_{NR}^{(3)}$; picosecond light pulses and delayed probing with tuning of the frequency difference $\omega_L - \omega_s$ are required (see [6.61–64]).

In the experiment of Fig. 6.6 the strong Raman band of CCl_4 at $\tilde{\nu} = 459\ cm^{-1}$ was investigated and the influence of the nonresonant susceptibility of the solvent cyclohexane was evident because of the high dilution of the CCl_4 molecules, which reduced the resonant contribution to the signal. There are many experiments, where $\chi_{NR}^{(3)}$ contributes to the probe signal even in concentrated samples. This situation occurs, when (i) weak Raman transitions are investigated, (ii) very strong nonresonant susceptibilities exist, as e.g. in semiconductors, or (iii) the excitation process is very transient, i.e. when the duration of the excitation pulses is much shorter than the dephasing time T_2. The latter case was realized under the experimental conditions of Fig. 6.5a, where the excitation pulses of $t_p = 70$ fs were considerably shorter than the dephasing time $T_2 = 1$ ps.

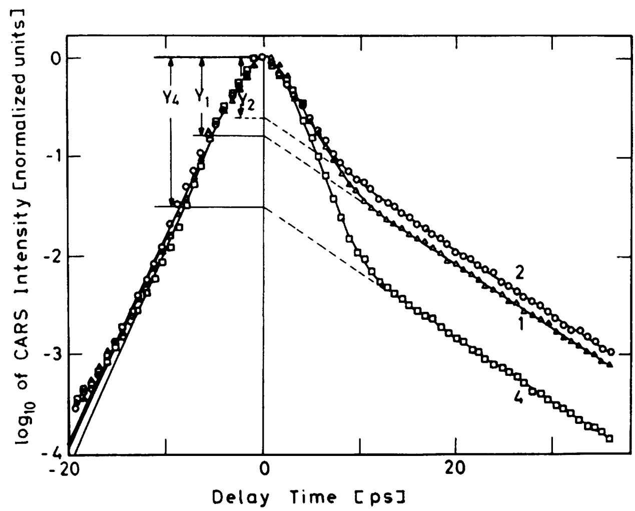

Fig. 6.7. Time-resolved CARS signal for LO-phonons in GaP measured for different polarization conditions showing the influence of the nonresonant susceptibility $\chi^{(3)}_{NR}$ (around time zero) and the exponential decay of the resonant signal at later delay times [6.65]

An interesting example, where a time-domain experiment allows determination of the components of the nonresonant susceptibility tensor $\chi^{(3)}_{NR}$ in crystalline gallium phosphate, GaP, is presented in Fig. 6.7 [6.65]. The coherent anti-Stokes signal was recorded for three different polarization conditions of excitation and probing fields (curves 1, 2, and 4 in Fig. 6.7). The slow exponential decay at later times corresponds to the LO-Raman resonance of GaP at 403 cm^{-1}. Each configuration of polarization of excitation and probing light fields yields the same dephasing time for the LO-phonons, but a different ratio between nonresonant and resonant part of the signal (represented by the values Y_i obtained after extrapolation of the resonant part back to time zero). A complete analysis of the data of Fig. 6.7 together with measurements at other polarization configurations has provided numbers for the components of the nonlinear susceptibility tensor $\chi^{(3)}_{NR}$.

c) Vibrational Transitions in Solids

Time-resolved coherent Raman scattering supplies valuable dynamical information on vibrations (phonons) in the solid phase at low temperatures. Here the relaxation times are often long, e.g. $T_2 \simeq 10^{-10}$ s, and the study of the corresponding line shapes (width $\Delta\nu/c \sim 0.1$ cm^{-1}) via spontaneous Raman scattering becomes difficult. On the other hand, time-resolved coherent experiments are readily made in this time domain. Due to the well-defined dispersion relations $\omega(k)$ of the phonons in crystalline solids, the time-resolved experiments require special care to properly adjust the polarization and propagation conditions to the symmetry of the investigated modes (see e.g. *Giordmaine* and *Kaiser* [6.1] and *Velsko* et al. [6.66]).

The relaxation time T_2 of vibrational modes in crystals has been treated theoretically in a number of publications [6.9,56,67–79]. It could be shown that the pure dephasing times increase with decreasing temperature proportional to $(T_D/T)^7$ for $T \ll T_D$, where T_D is the Debye temperature [6.67]. On the other hand, the energy relaxation time T_1 approaches a finite value at low temperatures and therefore determines the total phase relaxation $1/T_2 = 1/(2T_1)$ for $T \to 0$.

The equivalence of the coherent relaxation time τ to the energy relaxation times T_1 at low temperatures has been shown experimentally for molecular crystals, e.g. by echo experiments for pentacene in naphthalene and by measuring time-resolved spontaneous anti-Stokes Raman scattering for non-thermal LO-phonons in GaAs at 77 K [6.9,80,81].

Time-domain coherent Raman investigations exist for a number of crystals. In an early investigation the TO lattice mode of diamond was found to have a relaxation time $T_2/2$ of 3.4 ps and 2.9 ps at 77 K and 295 K, respectively [6.82]. Another example is given in Fig. 6.7, where GaP is investigated. The slow exponential decay of the coherent signal allows one to deduce the lifetime of the LO-phonon mode of GaP at $403\,\mathrm{cm}^{-1}$ A value of $T_2/2 = 6.7 \pm 0.3$ ps was reported [6.33]. In a recent paper, *Bron* et al. [6.83] studied the temperature dependence of T_2 of the LO-phonons of GaP and ZnSe by time-resolved coherent Raman scattering. The authors interpret their data as follows: At low temperatures the LO-phonons with wave vector $|k| \simeq 0$ decay into two acoustic phonons with half the energy and with equal wave vectors q_i of opposite sign, $q_1 = -q_2$. Impurity scattering was not relevant in the presence of nitrogen impurities of the order of $10^{16}\,\mathrm{cm}^{-3}$ in the GaP crystal. For elevated temperatures $T > 150$ K, higher-order phonon-phonon interactions begin to play a role.

The internal A_1 mode of α-quartz at $\nu/c = 465\,\mathrm{cm}^{-1}$ was investigated over a wide temperature range by *Gale* and *Laubereau* [6.84]. The experiments yielded a pronounced temperature dependence of the relaxation times, e.g. time constants of $T_2/2 = 0.8$ and 3.4 ps were found at 295 and 23 K, respectively. The phonon relaxation in α-quartz was discussed in terms of a three-phonon process, where the population of the excited $465\,\mathrm{cm}^{-1}$ phonon decays, generating an acoustic phonon at $\nu_1 = 51\,\mathrm{cm}^{-1}$ and an optical phonon at $\nu_2 = 414\,\mathrm{cm}^{-1}$ The temperature dependence of the decay time T_2 was successfully described by the relation $2/T_2 = \gamma[1 + n_1(T) + n_2(T)]$, where n_1 and n_2 are the thermal occupation numbers of the created phonons, γ is the low-temperature relaxation rate and T the temperature.

Besides the examples given above numerous publications have focused on other inorganic crystals. They have treated, for example, the dephasing of one-phonon states in calcite [6.30,85,86], of polaritons in ammonium chloride [6.87], or of two-phonon states [6.88–90].

A number of papers have addressed vibrational modes in organic molecular crystals [6.91–102]. In these materials the transition frequencies are often similar to those in molecular liquids. When several molecules are in the elementary cell, a splitting of the transition lines may occur due to the different local symmetry

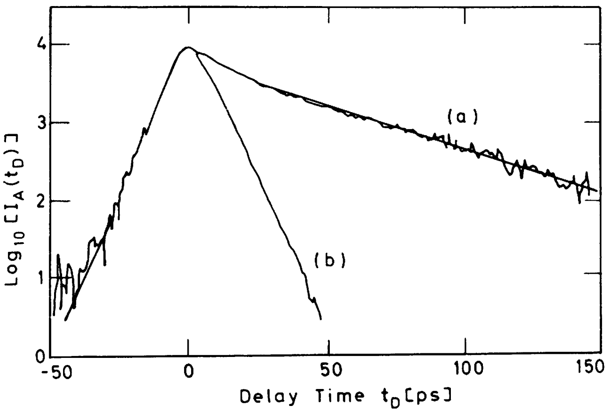

Fig. 6.8. Time-resolved CARS signal decay for the ν_1 mode, A_g factor group of crystallized benzene of natural isotope composition at 1.6 K. (*a*) Measured signal and best-fit curve. From the exponential decay a time constant of $T_2/2 = 40 \pm 2$ ps is deduced. (*b*) Instrumental response function [6.97]

of the molecules (factor group splitting). Extensive investigations of the relaxation processes in crystalline benzene were carried out by *Hochstrasser*'s group [6.96–101].

An example is given in Fig. 6.8, curve *a*, where the coherent anti-Stokes signal at 1.6 K is plotted as a function of the time delay t_D for the A_{1g} factor group of the ν_1 mode ($\nu/c = 991\ \text{cm}^{-1}$) of benzene with natural carbon isotopic composition (curve *b* gives the instrumental response) [6.97]. The signal decays exponentially with a time constant of $\tau = T_2/2 = 40 \pm 2$ ps at later delay times. Extrapolating the exponential slope back to time zero one finds a slight contribution from the nonresonant susceptibility $\chi^{(3)}_{NR}$. A number of additional experiments were carried out with benzene at low temperatures in order to deduce the relevant relaxation mechanism. Measurements of different factor groups indicated faster decay times of $\tau = 35.6$ ps for the B_{2g} component [6.99]. Mixed crystals containing C_6D_6 molecules gave increased decay rates [6.97]. Important for the understanding of the relaxation mechanism is the finding that the decay rates depend on the isotopic composition of carbon in the benzene molecule. It should be noted that natural benzene contains 1.1% of ^{13}C carbon. Experiments have been performed with neat $^{12}C_6H_6$ benzene crystals giving considerably longer decay times of $T_2/2 = 61.7$ ps (A_{1g}) and $T_2/2 = 56$ ps (B_{2g}). Strong isotope effects have also been found for a number of other vibrational modes of benzene crystals [6.99].

The low-temperature relaxation rates of the isotopically pure benzene crystals show mode specific energy relaxation. The ^{13}C "impurities" in the molecules cause increased relaxation rates due to impurity phonon scattering or near resonant ($\Delta E \sim 9\ \text{cm}^{-1}$) energy trapping. The experiments with benzene crystals demonstrate that the relaxation rates measured via time-resolved coherent Raman scattering give a lower value for the energy relaxation time T_1 in the isotopically mixed samples, while they give T_1 in the pure crystals. These observations provide convincing evidence that the isotopic composition of the molecules has to be taken into account when interpreting the phonon relaxation.

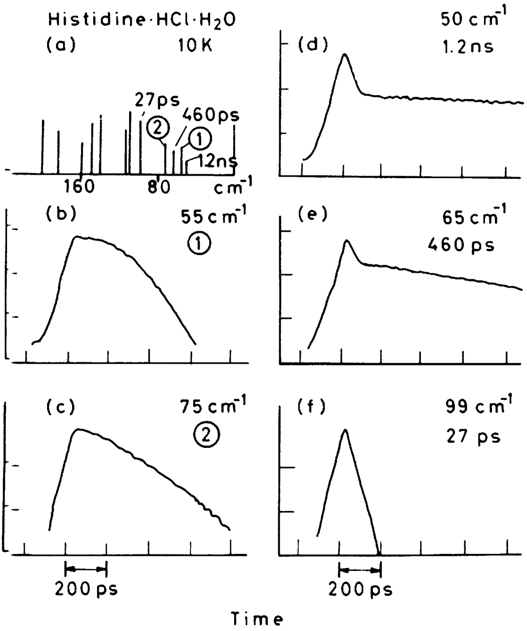

Fig. 6.9a–f. Time-resolved coherent Raman data for 1-(*t*)-histidine. HCl · H_2O crystals at 10 K (semi-log plots). (**a**) Positions of the low-frequency modes. (**b**)–(**f**) Time-resolved data for the five low-frequency modes shown in (**a**). Exponential decays are found for the totally symmetric modes at 99 cm^{-1}, 65 cm^{-1}, and 50 cm^{-1}, whereas the two modes at 55 cm^{-1} (**b**) and 75 cm^{-1} (**c**) suggest inhomogeneous line-broadening [6.102]

Of special interest are time-resolved coherent Raman investigations in large molecules which are of biological relevance. Extensive investigations of low-frequency vibrational modes (librons) in crystals of aminoacids and peptides were reported by *Dlott* [6.79]. An example is presented in Fig. 6.9, where crystals of L-histidine hydrochloride monohydrate were investigated at 10 K [6.102]. The frequency positions, the intensities, and the observed lifetimes are summarized schematically in Fig. 6.9a. A common feature of the relaxation properties of the vibrations in the aminoacid crystals is the following: Modes with frequencies higher than 150 cm^{-1} show lifetimes $\tau = T_1$ shorter than 10 ps. For the symmetric modes the lifetimes increase with decreasing frequency ω_0. The relaxation data for the totally symmetric 99, 65, and 50 cm^{-1} lattice modes are depicted in Fig. 6.9d–f, where the lifetimes extend up to $\tau = 1.2$ ns. From the frequency dependence of T_1 the authors concluded that the decay times are determined by spontaneous decay of librons into two counterpropagating acoustic phonons or into one libron and one acoustic phonon. The non-totally symmetric local modes at 55 and 75 cm^{-1} show non-exponential (Gaussian) decay (see Fig. 6.9b,c). The inhomogeneous broadening of these local modes is believed to be due to dipolar interactions or small variations in the crystal packing.

A short summary should be given here concerning the coherent relaxation times and the relaxation mechanisms found in molecular crystals:

i) Homogeneously broadened lines are frequently found. The inhomogeneity which one would expect due to the site-specific frequency shifts appears in most systems as factor group splitting. It is commonly accepted that imperfections o the crystals are less effective due to the delocalisation of the phonons (motional narrowing); but they may strongly affect the relaxation processes.

ii) The frequency widths or time constants at elevated temperatures are determined by energy relaxation, dephasing or intraband relaxation, and impurity scattering. In a number of cases the temperature dependence of the time constant allows one to determine the relaxation mechanism.

iii) At very low temperatures the relaxation rates become constant. They are determined by energy relaxation and impurity scattering. The decay times measured in coherent experiments give directly the energy relaxation time T_1. Care has to be taken when impurities influence the coherent decay times; in this case only a lower limit for T_1 may be estimated.

d) The Collision Time

We return now to molecular modes in liquids. The theoretical model of Section 6.1 treated the relaxation processes in terms of two time constants, T_1 and T_2 At very early times, $t_D \ll T_2$, however, the time-dependent interaction during the collisions of the molecules becomes important. As a consequence, the correlation function $\langle\langle q(0)q(t)\rangle\rangle$ is no longer a single exponential, but has the form [6.3,4,50,103]:

$$\langle\langle q(0)q(t)\rangle\rangle \propto \exp\left\{-\frac{t}{T_2}-\frac{\tau_c}{T_2}\left[\exp\left(-\frac{t}{\tau_c}\right)-1\right]\right\}\,. \qquad (6.15)$$

Equation (6.15) was derived by Kubo for an exponential decay of the frequency correlation function, $\langle\delta\omega(t)\delta\omega(0)\rangle = \exp(-t/\tau_c)$. The collision time τ_c is the time for which a certain frequency shift $\delta\omega(t) = \omega(t) - \omega_0$ is maintained.

At later times (6.15) gives the exponential decay of the coherent amplitude with $\exp(-t/T_2)$, while at short times, $t \to 0$, (6.15) implies a Gaussian time dependence $\exp[-t^2/(T_2\tau_c)]$. For short collision times $\tau_c \ll T_2$ the collision process leads to small corrections of the coherent signal. Nevertheless, time-resolved coherent scattering may be used to determine the collision time τ_c or can enable one to estimate an upper limit for τ_c. For an example we refer to Figs. 6.4b and 6.5. The decay of the coherent signal was found to be exponential for times larger than 0.3 ps. Taking into account the accuracy of the experimental data and the nonresonant susceptibility $\chi^{(3)}_{\mathrm{NR}}$, one may estimate an upper limit for the collision time of both acetone modes and for the acetonitrile mode of $\tau_c < 0.3$ ps.

For sufficiently long collision times $\tau_c \geqslant 0.5$ ps, picosecond light pulses from a Nd:glass laser may be used for the direct determination of τ_c. *Telle* and *Laubereau* have performed coherent experiments with a carefully controlled time resolution of the experiment [6.104]. They simultaneously measured the temporal response of their system (by coherent scattering of a purely nonresonant susceptibility) and the coherent signal of the investigated transition (liquid CH_2BrCl). From the experimental curves and numerical calculations based on the (measured) temporal system response the authors estimated a collision time of

$$t_c = 0.4\begin{pmatrix}+0.4\\-0.1\end{pmatrix}\mathrm{ps}\ , \qquad \text{i.e. } 0.3 - 0.8\,\mathrm{ps}\ .$$

In a recent paper *Chesnoy* investigated the kinetics of vibrational dephasing of nitrogen under supercritical conditions [6.41]. He demonstrated that, after some initial delay, the coherent signal decays exponentially with time. Comparing the time-resolved coherent Raman data with spontaneous Raman spectra enabled a collision time of $\tau_c \simeq 10\,\mathrm{ps}$ to be deduced; this is of the same order as the measured dephasing time of $T_2 \simeq 20\,\mathrm{ps}$. The long collision time τ_c indicates the importance of density fluctuations as a source of frequency modulation close to the critical point.

6.2.2 Time-Resolved Coherent Raman Scattering of a Distribution of Resonance Frequencies

a) Time-Domain Experiments

In the previous sections we discussed time-resolved coherent investigations, where dynamic processes such as dephasing and energy relaxation were of major relevance. Here we address new spectroscopic studies which allow accurate measurement of frequency differences between vibrational modes and the resolution of transitions within congested spectral regions.

The following time-resolved coherent experiments are described by (6.1–13) discussed above. For each vibrational mode one introduces individual coherent amplitudes Q_j and vibrational resonance frequencies ω_j. The coherently scattered field is a sum of field components scattered from the individual molecular modes Q_j [6.7,37,105].

$$E_A(t,t_D) = \sum_j E_{Aj}(t,t_D) \propto \sum_j Q_j(t)E_{L2}(t - t_D)\exp(-\mathrm{i}\omega_j t)\ . \tag{6.16}$$

The observed coherent signal has the form $S(t_D) \propto \int dt|E_{AS}(t,t_D)|^2$. It can be shown that in the limit of short excitation and probing pulses the signal $S(t_D)$ at $t_D > 0$ is proportional to the absolute square of the Fourier transform of the spontaneous Raman spectrum $R(\omega)$, i.e. $S(t_D) \propto |\int d\omega \exp(\mathrm{i}\omega t_D)R(\omega)|^2$ [6.3,105]. In the time domain – according to (6.16) – simultaneously excited modes lead to a beating of the coherent signal at the frequency differences $\delta\omega_{ij}$ between the various transition frequencies ω_i and ω_j, with $\delta\omega_{ij} = \omega_i - \omega_j$. These "quantum" beats of the coherent signal were found for the first time by *Laubereau* et al. [6.36] in a number of tetrahalides. Later, similar beating phenomena were reported in several publications [6.37,44,94,98,102,106–108].

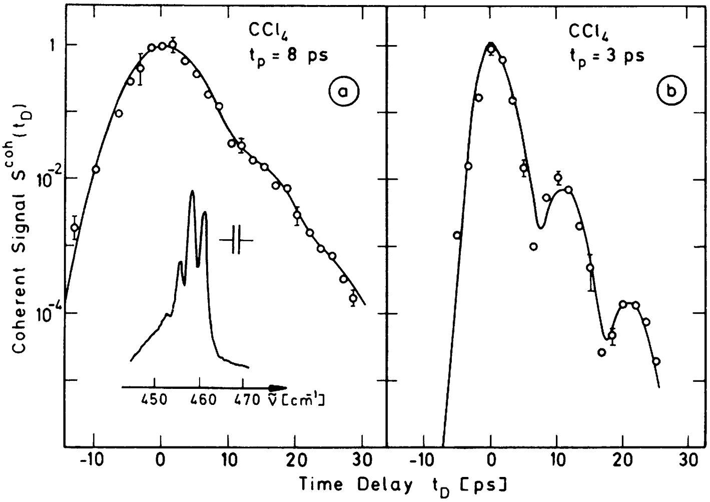

Fig. 6.10a, b. Coherent Stokes signal from the ν_1 mode of liquid CCl_4. The isotope composition of CCl_4 leads to a splitting of the ν_1 band in the spontaneous Raman spectrum – see insert in (**a**). The different resonance frequencies lead to the beating phenomenon which is clearly resolved in (**b**) where exciting and probing pulses of 3 ps duration were used. For longer ($t_p = 8$ ps) pulses the beating structure is smeared out. Nevertheless, the dephasing time T_2 is readily determined in both experiments [6.57]

Figure 6.10 presents the results of a study of the ν_1 mode of liquid carbontetrachloride ($\nu/c \simeq 459\,\mathrm{cm}^{-1}$) where the influence of the pulse duration on the observed beating was investigated [6.37]. Due to the natural isotopic composition of the CCl_4 molecules (the two chlorine isotopes ^{37}Cl and ^{35}Cl have abundances of 24% and 76%, respectively), the transition is split in five equidistant components (distance $\Delta\nu/c = 3\,\mathrm{cm}^{-1}$). Four of the more abundant components are readily resolved in the spontaneous Raman spectrum as shown in the insert of Fig. 6.10a. In the time-resolved coherent experiment one expects a beating phenomenon with maxima separated by $\Delta t = 1/\Delta\nu \simeq 11$ ps. This beating is indeed observed in Fig. 6.10b, where short excitation and probing pulses with $t_p = 3$ ps were used. In addition, one obtains information on the dephasing time T_2. The solid curve was calculated using the measured pulse parameters ($t_p =$ 3 ps, Gaussian shape), a difference of the neighboring frequency components of $3.0\,\mathrm{cm}^{-1}$, a dephasing time $T_2 = 6$ ps (assumed to be the same for all components) and the nonresonant susceptibility $\chi_{NR}^{(3)}$. Figure 6.10a shows the signal curve for longer excitation and probing pulses ($t_p \simeq 8$ ps). Here the beating phenomenon is smeared out and the decay, with the time constant $T_2 = 6$ ps, appears quite clearly. The longer pulses influence the signal curve in two ways: (i) During the longer excitation process the most intense transition of the Raman spectrum is preferentially excited, and (ii) the long duration of the probing pulse gives a levelling of the modulation. The two experiments of Fig. 6.10 show convincingly

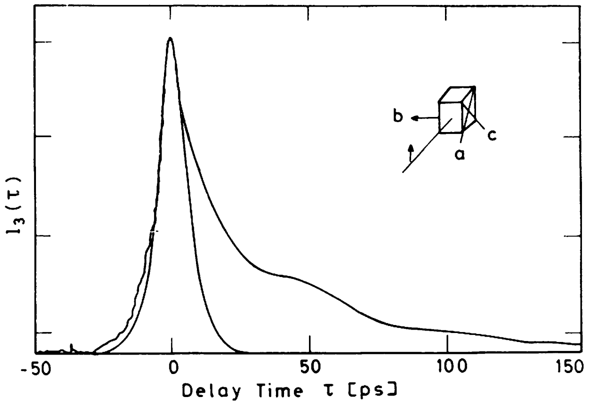

Fig. 6.11. Time-resolved coherent Raman data for a special phase-matching condition, where the A_g and the B_{2g} factor group components of the 991 cm^{-1} vibron of crystallized benzene are probed simultaneously. The modulation of the signal is due to the frequency shift of 0.64 cm^{-1} between the two interfering lines. Also shown is the experimental response function [6.98]

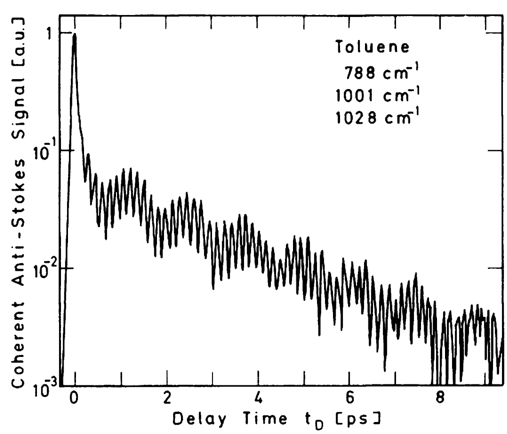

Fig. 6.12. Terahertz beats observed in time-resolved coherent Raman scattering from liquid toluene using femtosecond light pulses. The interference of the three simultaneously excited toluene modes at 788, 1001, and 1028 cm^{-1} generates a rich structure with beat frequencies up to 7.2 THz [6.106]

that time-resolved coherent experiments are well suited to investigate frequency differences and decay times in spectral regions consisting of discrete frequency components.

Beating between transitions of different factor groups was studied by *Velsko* et al. [6.98] in crystallized benzene at low temperature (1.6 K). Some results are shown in Fig. 6.11. The geometry of the excitation and probing light field was selected in such a way that coherent signals were obtained from the A_g and B_{2g} states in the factor groups of the 991 cm^{-1} transition of benzene. From the beating of the signal (i.e. the time between the peaks) and from its magnitude the authors determined the frequency difference to be $\Delta\nu = 19$ GHz, the relative amplitudes to be 20 : 1, and the decay times of the two modes to be 40 and 34 ps, respectively.

While the experiment on crystallized benzene gave beating frequencies in the 20 GHz range, the advent of femtosecond light pulses allows one to measure beating frequencies far into the terahertz regime. Beat frequencies of more than 10 THz have been reported [6.44]. Figure 6.12 shows very recent data from a coherent Raman experiment on liquid toluene [6.106]. In the wide frequency range of 700–1100 cm^{-1} three vibrational modes are excited simultaneously by the (broadband) femtosecond light pulses. The scattered coherent anti-Stokes signal exhibits an amazing beating structure with beat frequencies of up to 7.2 THz. The frequency components of the signal curve are evaluated by Fourier transformation or other more specialized numerical methods in order to obtain the spectral information. This procedure called "Fourier transform Raman spectroscopy" was first demonstrated by Graener and Laubereau [6.107]. The authors studied coherent beating in gaseous methane-argon mixtures on a much longer time scale of many picoseconds to nanoseconds.

It should be noted here that the case of continuously distributed resonance frequencies (e.g. an inhomogeneously broadened transition) leads to a more difficult situation. There is no recurrence of the signal but only destructive interference with a rapid signal decay. An early attempt to measure T_2 in inhomogeneously broadened frequency distributions by using a "selectivity in k-space" had to be reconsidered [6.36,109–114]. *Zinth* et al. showed experimentally that with the existing dispersion of the samples, a selectivity for a molecular subgroup is not possible [6.37]. In addition, general theoretical arguments prove that the information from a single-pulse coherent experiment and from a spontaneous Raman spectrum is equivalent [6.103,115,116]; i.e. T_2 cannot be obtained in a coherent Raman experiment, where the spontaneous Raman line is strongly inhomogeneously broadened.

Under certain conditions, however, time-resolved coherent Raman techniques may give information on the line-broadening mechanism. Two processes cause similar non-Lorentzian spontaneous Raman bands: (i) Long collision times $\tau_c \simeq T_2$ and (ii) inhomogeneous broadening (cross-relaxation times much longer than T_2).

Gale et al. [6.42] pointed out that coherent experiments give new information on the broadening mechanism: (i) If τ_c is relatively long, $\tau_c \simeq T_2$, the coherent signal decays non-exponentially around time zero but turns to an exponential decay at later times. (ii) For a small inhomogeneous contribution an initial exponential decay with time constant $T_2/2$ (close to time zero) is followed by an increasingly rapid decay at later times [6.105]. If the inhomogeneous width adds 10% to the homogeneous linewidth, the slope of the signal decay (on a semilog plot) gives $T_2/2$ around time zero. This slope increases with time. For example, four orders of magnitude below the signal peak, the slope is larger than at time zero by more than 50%. While the influence of weak inhomogeneous broadening [case (ii)] and of long collision times τ_c [case (i)] yield very similar spontaneous Raman spectra, the time-resolved coherent data are different and may be used to decide which line-broadening mechanism exists.

b) Transient Frequency-Domain Experiments

In the previous section we discussed investigations where the spectral information on the molecular system was deduced from time-resolved coherent data followed by a numerical analysis. Now we present a technique which avoids the Fourier transformation by directly measuring the spectrum of the coherent signal generated by properly shaped probing pulses [6.64,117–121].

The basic idea of the technique is readily seen by considering the spectrum of the scattered coherent anti-Stokes signal of a single vibrational transition

$$I_A(\omega) \propto \left| \int dt \exp(i\omega t) E_A(t) \right|^2 \tag{6.17a}$$

$$I_A(\omega) \propto \left| \int dt \exp(i\omega t) E_{L2}(t) \exp\left(-\frac{t}{T_2}\right) \right|^2 \tag{6.17b}$$

$$I_A(\omega) \propto \left| \int dt \exp(i\omega t) \exp\left[-\left(\frac{t}{t_0}\right)^2 - \frac{t}{T_2}\right] \right|^2 \tag{6.17c}$$

$$I_A(\omega) \propto \left| \int dt' \exp(i\omega t') \exp\left[-\left(\frac{t'}{t_0}\right)^2\right] \right|^2 . \tag{6.17d}$$

In these equations it is assumed that the excitation and the initial effects of the collision process are terminated. Equation (6.17a) represents the Fourier transform of the anti-Stokes signal. The freely relaxing coherent amplitude $Q = Q_0 \exp(-t/T_2)$ is monitored by a Gaussian shaped laser field $E_{L2}(t) \propto \exp(-t^2/t_0^2)$ [see (6.17b,c)]. By introducing a new time t', one eliminates the dephasing time. According to (6.17d), the anti-Stokes spectrum has the same frequency shape, i.e. the same frequency bandwidth, as the probing laser pulse E_{L2}. With the phase factors included in (6.17) one finds the anti-Stokes band centered at the anti-Stokes frequency $\omega_{AS} = \omega_{L2} + \omega_0$. When sufficiently long ($t_p > 1.5\, T_2$) probing pulses of Gaussian shape are used, the spectral width $\Delta\nu$ of the time-resolved coherent anti-Stokes band, $\Delta\nu = 0.44/t_p$, is narrower than the spontaneous Raman line $\Delta\nu = 1/\pi T_2$. In practical applications it is advantageous to use a short exciting force and a prolonged Gaussian shaped interrogation pulse. As an acronym the spectroscopic technique is known as SEPI spectroscopy. A more detailed description of the theory is given in the literature by *Zinth* et al. [6.119] and *Collins* et al. [6.122].

An experimental example of the line-narrowing SEPI spectroscopy is given in Fig. 6.13. The ν_1 mode of liquid CCl_4 was investigated using a Nd:glass laser system supplying 20 ps probing pulses of Gaussian shape. In Fig. 6.13a the spontaneous Raman spectrum of the ν_1 mode is shown as measured with a high-resolution Raman spectrometer; the isotopic structure has been discussed above. The SEPI spectrum (Fig. 6.13b) was taken by using a high-resolution spectrograph in conjunction with an optical spectrum analyser. The entire coherently scattered spectrum is recorded immediately for each probe pulse. When the excitation force (i.e. $E_L E_s^*$) is centered at 460 cm^{-1} (see Fig. 6.13b), the two high-frequency components of the isotopically split Raman band appear very narrow and thus well resolved. The SEPI spectrum clearly separates the two

Fig. 6.14 ▶

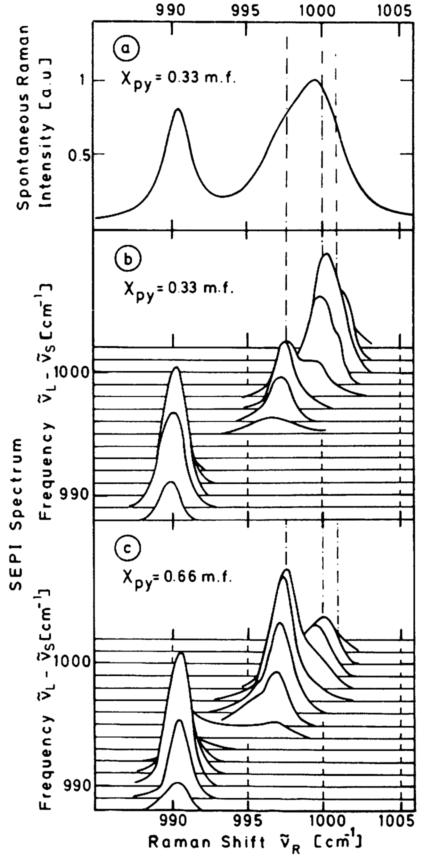

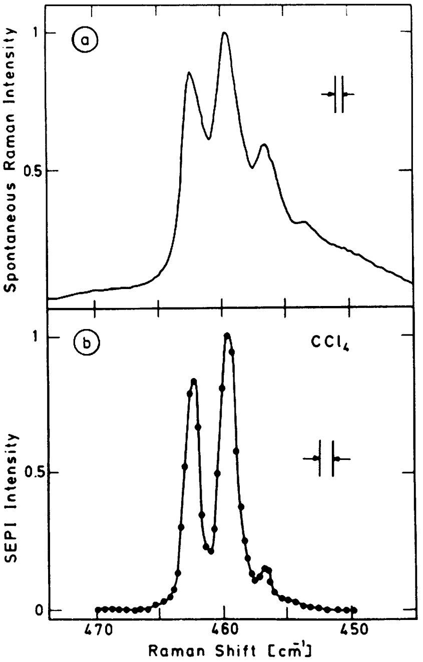

▲

Fig. 6.13a, b. Line-narrowing coherent Raman spectroscopy using short excitation and prolonged coherent interrogation (SEPI) of the ν_1 mode of liquid CCl_4. Broad overlapping lines of the spontaneous Raman spectrum (**a**) are considerably narrowed by the coherent SEPI technique (**b**) [6.105]

Fig. 6.14a–c. Raman spectra of pyridine: methanol mixtures. (**a**) Polarized spontaneous Raman spectrum measured at a pyridine concentration of 0.33 molar fraction taken with a standard Raman spectrometer of spectral resolution of $0.5\,\mathrm{cm}^{-1}$. (**b**) and (**c**) Short excitation and prolonged interrogation (SEPI) spectra obtained for a set of excitation frequencies, $\nu_L - \nu_s$, at two pyridine concentrations, $\chi_{py} = 0.33$ molar fraction (**b**) and $\chi_{py} = 0.66$ molar fraction (**c**). The spectra taken at excitation frequencies $\nu_L - \nu_s < 994\,\mathrm{cm}^{-1}$ are drawn with reduced amplitudes. The SEPI spectra resolve three Raman lines of different hydrogen-bonded aggregates hidden under the broad band of the spontaneous Raman spectrum (see dash-dotted lines) [6.120]

bands and allows a very accurate determination of the frequency difference of $\delta\nu/c = 3.0 \pm 0.08\,\mathrm{cm}^{-1}$.

An interesting application of the line-narrowing SEPI spectroscopy is presented in Fig. 6.14 [6.120]. The molecular system pyridine: methanol was investigated, which exhibits a broad featureless spontaneous Raman band around

$1000\,\mathrm{cm}^{-1}$ (see Fig. 6.14a). The position and amplitude of this band changes with varying methanol concentration. With the help of a picosecond dye laser system, the frequency of the excitation force was tuned over the frequency range of interest. SEPI spectra taken at fourteen excitation frequencies are shown in Fig. 6.14b, c for two different methanol concentrations. In both cases the band at $1000\,\mathrm{cm}^{-1}$ can be resolved in three components at 997.3, 1000.0, and $1001\,\mathrm{cm}^{-1}$. The positions of the three bands remain constant while the amplitudes depend on the methanol concentration. From these data new information on hydrogen-bonded complexes between pyridine and methanol were obtained: there exist at least three distinct molecular complexes of pyridine and methanol with frequency positions remaining constant with methanol concentrations. The apparent frequency shift of the Raman band observed in spontaneous spectroscopy results from the changing abundance of the complexes as a function of the methanol concentration.

The following points concerning the line-narrowing transient Raman spectroscopy are of interest:

i) The SEPI method investigates the freely relaxing molecules.
ii) Influences of $\chi^{(3)}_{\mathrm{NR}}$ are eliminated as the probing process is performed at late delay times.
iii) We emphasize that the amplitudes of the SEPI bands depend on the Raman cross sections and also on the dephasing times T_2 of the individual modes. This fact provides increased spectral resolution in congested spectral regions when fast decaying bands disappear at late delay times.
iv) The SEPI experiments may be performed with coherent anti-Stokes or Stokes scattering. The two spectra give the same information.

6.2.3 Resonant Pulse Propagation in the Infrared

In the previous sections the discussion concentrated on Raman-type interactions. The absence of a dipole moment required a pair of light pulses for the excitation of the molecules and a separate probing pulse to study the time evolution of the material excitation. In this section we focus on infrared-active transitions where the material is excited by resonant ir light and where the oscillating molecules emit radiation. We discuss the case of a single small area excitation pulse propagating resonantly through the absorbing medium [6.7, 123–125].

It has been shown in [6.7] that small area pulse propagation may be treated by a single equation containing the dephasing time T_2 and a modified Bessel function. The discussion may be further simplified for the case of optically thin samples, i.e. where the absorbance $a = \alpha l$ = (absorption coefficient × sample length) is small, $a \ll 1$. The transmitted electric field may then be written as follows [6.125]:

$$E_{\mathrm{tr}}(t) = E_0(t) - \frac{\alpha l}{2T_2} \int_{-\infty}^{t} dt' E_0(t') \exp\left[\left(t' - t\right)\left(\frac{1}{T_2} - \mathrm{i}\Delta\right)\right] . \tag{6.18}$$

As previously, Δ stands for the difference between resonance and driving frequency. According to (6.18) the transmitted electric field consists of the incoming light field minus a second term which decays with the dephasing time T_2. Thus the dephasing time T_2 can be directly measured from the slope of the trailing part of the transmitted, i.e. coherently emitted, light field. In the general case of $\alpha l \gtrsim 1$ the trailing part of the signal decays more rapidly. For values $\alpha l = 1$ a simple correction formula may be used in order to deduce T_2 from the measured decay [6.126].

An elegant experimental system to measure the small area pulse propagation in the infrared was developed by *Hartmann* and *Laubereau* [6.124]. The main difficulty which had to be overcome was the slow time resolution of the photodetectors. Existing infrared detectors are not able to measure the transmitted pulse with picosecond time resolution. The detection of the pulse intensity as a function of time is accomplished by gated ultrafast infrared up-conversion. This technique provides the convolution of the instantaneous infrared intensity with a short probing pulse. Tuning the time delay between the exciting infrared pulse and the probing gate pulse allowed the evolution of the coherently radiated infrared signal to be followed.

In a recent experiment, the coherent interaction of an infrared pulse with rotational transitions of HCl:Ar gas mixtures at medium pressure was studied [6.127]. HCl was used with natural isotope abundance of the ^{35}Cl and ^{37}Cl isotopes. Transitions of the $R(J)$ branch of HCl around 3000 cm^{-1} were investigated for different values of the rotational quantum number J of the $J \rightarrow J + 1$ rotation-vibrational transition. An example is presented in Fig. 6.15. The infrared

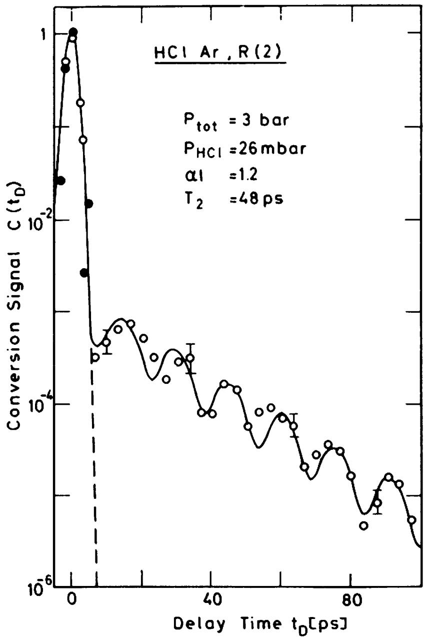

Fig. 6.15. Resonant propagation of an infrared pulse through a HCl:Ar mixture. The conversion signal representing the transmitted and reemitted infrared intensity is plotted versus delay time t_D. Note the beating in the reemitted part at $t_D > 10$ ps which is due to the interference from the emission from the $R(2)$ transition of HCl containing the two chlorine isotopes ^{35}Cl and ^{37}Cl. From the decay of the signal a dephasing time $T_2 = 48 \pm 5$ ps was determined [6.127]

pulse is tuned to the $R(2)$ transition of $H\,^{35}Cl$. The related $R(2)$ transition of $H\,^{37}Cl$ is shifted by $\simeq 2\,\mathrm{cm}^{-1}$ to smaller frequencies but also interacts with the incident pulse. [For the numerical analysis of the experimental data the second transition has to be incorporated in (6.18)]. The time integrated conversion signal $C(t_D)$ is plotted in Fig. 6.15 on a logarithmic scale as a function of the delay time of the probing pulse. Around $t_D = 0$ the conversion signal of the emitted pulse (open circles, solid line) follows the input pulse (full circles, broken line). For longer delay times, $t_D > 10\,\mathrm{ps}$, the emitted pulse decays more slowly. A beating phenomenon (beat time 15.3 ps) is found which is superimposed on an approximately exponential decay ($\tau = 19.5\,\mathrm{ps}$). The analysis of the data – taking into account the optical thickness of the sample, $\alpha l = 1.2$ – yielded a frequency distance between the isotope components of $2.18\,\mathrm{cm}^{-1}$ and the dephasing time of $T_2 = 48 \pm 5\,\mathrm{ps}$. Measurements at different partial pressures of HCl and Ar gave the following results: HCl–HCl collisions are much more efficient for the dephasing process than HCl–Ar collisions; the relaxational data for the rotational-vibrational transitions of HCl agree well with the relaxation data for pure rotational transitions, suggesting that vibrational relaxation contributes little to the observed dephasing process. The authors proposed that total dephasing is due to pure rotational dephasing (quasi-elastic collisions) and the population decay of the rotational levels (inelastic collisions).

6.3 Coherent Spectroscopy Using Multiple Excitation Processes

In the preceding sections we have discussed various applications of coherent spectroscopy using a single excitation process. One major result was the determination of the dephasing time T_2 in a variety of systems. On the other hand, these techniques do not allow measurement of the dephasing time T_2 for wide inhomogeneously broadened lines and give no information on the energy relaxation time T_1 (except in solids at low temperature).

In the theoretical part (Sect. 6.1.3) it was shown that multiple excitation experiments provide additional information. These experiments, frequently called echo experiments, have their analogues in magnetic resonance. They have been demonstrated for optical transitions, initially on a nanosecond or even longer time scale [6.11–13]. More recently, picosecond and femtosecond measurements have been reported. Successful echo experiments require a pulse area A of approximately one. For small pulse areas, the echo signal is drastically reduced, since the signal intensity is proportional to A^6. For this reason ultrafast echo experiments are only possible when the relaxation times T_1 and T_2 are sufficiently long and when the transition dipole moment μ is large. Since 1975 ultrafast echo experiments have been performed on electronic transitions in dye solutions [6.128–130], in low-temperature solids (e.g. excitons in semiconductors [6.131, 132] and molecular crystals [6.9,133–139] on a picosecond time scale or, more recently, in dye solutions with femtosecond pulses [6.140–142]. A number of theoretical papers treat the different echo techniques [6.143–147].

In the literature different – and in some cases misleading – names have appeared for the same coherent experiment. We briefly discuss (i) the echo experiments and (ii) the induced grating experiments, two aspects of the same coherent investigation.

i) In a coherent experiment with multiple excitation pulses, the system is excited (at time zero) by a first pulse (wave vector $\boldsymbol{k}_a$). After an evolution time t_1 a second excitation pulse (wave vector $\boldsymbol{k}_b$) passes through the sample and interacts with the excited molecules. Rephasing of the excited molecule leads (in the case of inhomogeneous broadening) to the formation of a delayed radiation – the echo. The echo is emitted at a time $t = t_1$ after the second pulse under the well-defined phase-matching condition with wave vector $\boldsymbol{k}_e = 2\boldsymbol{k}_b - \boldsymbol{k}_a$.

ii) In the excitation process, the polarization produced by a first excitation pulse and part of the second pulse, form an excitation grating in the sample (the induced grating) with the wave vector $\boldsymbol{k}_g = \boldsymbol{k}_b - \boldsymbol{k}_a$. The trailing part of the second pulse or a third pulse (see Sect. 6.3.2) interacts with the grating, generating radiation at the wave vector $\boldsymbol{k}_s = \boldsymbol{k}_b + \boldsymbol{k}_g = 2\boldsymbol{k}_b - \boldsymbol{k}_a$. This radiation – which forms the echo – is emitted with a time delay of $t = t_1$ in the case of inhomogeneously broadened transitions.

6.3.1 Ultrafast Two-Pulse Echo Spectroscopy

In the theoretical part [Eq. (6.7) in Sect. 6.1.2] a formal solution for the evolution of a two-level system was derived for the limiting case of light pulses with duration t_p much shorter than the system's time constants T_1 and T_2. In the case of a two-pulse echo, two pulses of area A_a and A_b are applied to the sample with a time separation of t_1. The resulting echo polarization is given by (6.9). The signal amplitude is proportional to $\sin A_a \sin^2(A_b/2)$ and decays with the dephasing time T_2. The emission direction is determined by the wave vector $k_e = 2k_b - k_a$. An important point emerges from the underlined part of (6.9): in the case of a wide inhomogeneously broadened transition the signal is emitted close to time $t = t_1$, i.e. the emission occurs delayed as a photon echo.

In a standard two-pulse echo experiment the echo energy, i.e. the time integral of the absolute square of the echo amplitude, is measured as a function of the separation t_1 between the two excitation pulses. In the case of a broad inhomogeneous line the signal is emitted only close to $t = t_1$ and its intensity decays with $\exp(-4t_1/T_2)$. For homogeneously broadened transitions the signal is emitted starting at $t = 0$. The decay (as a function of t_1) follows $\exp(-2t_1/T_2)$. (For intermediate line broadening see [6.14]). In order to obtain the dephasing time independently of the nature of the line broadening, only the polarisation at the time $t_e = t_1$ should be measured (this may be done by optical gating techniques). Under these conditions the signal depends on t_1 as $\exp(-4t_1/T_2)$ and is independent of the line shape.

The preceding discussion shows that the two-pulse echo technique allows determination of the dephasing time T_2 even for inhomogeneously broadened transitions, where experiments with single excitation pulses fail.

A number of two-pulse echo experiments have been performed on exciton bands of molecular crystals at low temperature. For instance, the relaxation of the 0–0 transition of pentacene in naphthalene (and in p-terphenyl) was studied as a function of temperature by *Hesselink* and *Wiersma* [6.9, 133]. Here the energy relaxation times T_1 are much longer ($\simeq 20\,\text{ns}$) than the dephasing times T_2 and the pure dephasing times T_2^* could be readily determined from the relation $1/T_2 = 1/T_2^* + 1/(2T_1) \simeq 1/T_2^*$. The temperature dependence of T_2^* was fitted with a relaxation theory involving low-energy ($\nu/c \simeq 16\,\text{cm}^{-1}$) pseudo-local phonons coupled to the pentacene transition. The experiment clearly demonstrated the importance of this relaxation channel for the dephasing of the excitonic transitions.

Recently, the two-pulse echo technique has been applied to two-dimensional excitons in GaAs-AlGaAs quantum wells by *Schultheis* et al. [6.132]. The authors used a synchronously pumped dye laser emitting pulses (with 12.6 ps autocorrelation width) tunable in the range of the exciton absorption band between $\lambda = 820\,\text{nm}$ and $\lambda = 750\,\text{nm}$. A pair of pulses at the temporal separation t_1 with wave vectors $\boldsymbol{k}_a$ and $\boldsymbol{k}_b$ was focussed into a sample consisting of 78 alternating layers of GaAs and AlGaAs (thickness 102 Å and 200 Å, respectively), grown by molecular beam epitaxy. The sample was kept at 2 K. The transmission spectrum of the inhomogeneously broadened exciton band is shown in the insert of Fig. 6.16 (broken curve). The echo signal was detected in the phasematching direction $2\boldsymbol{k}_b - \boldsymbol{k}_a$ with the help of a lock-in system. A series of data is shown in Fig. 6.16. The echo signals are plotted as a function of delay time t_1 for three different energies of the excitation photons. Curve *a* investigates the exciton at the low-energy side of the absorption band, curve *b* was measured at somewhat higher energies, and curve *c* was taken close to the peak of the exciton absorption.

The relaxation times of the sample do not fulfill the limit of $T_2 \ll t_p$ as assumed in the theoretical discussion of (6.19). A more detailed analysis was required in order to derive the relaxation time T_2 from the experimental curve. Together with T_1-data from hole-burning experiments, the analysis yielded interesting numbers. Close to the peak of the exciton band (curve *c*) the relaxation times are fast; $T_2 \simeq 4\,\text{ps}$ and $T_1 = 8\,\text{ps}$. Consequently, the diffracted signal intensity is small and the signal decay is very rapid. At the low-energy side of the exciton band the energy relaxation time T_1 is much longer (100 ps), while the dephasing increases to 22 ps. There is no change of the time constants T_1 and T_2 at the frequency positions *a* and *b* in the low-energy tail of the exciton band. The results are interpreted as follows: Near the peak of the exciton band, there are several contributions to the coherent decay: scattering with acoustic phonons, impurities and well thicknesses (spectral diffusion). Below the absorption peak, excitation is more localized and spectral diffusion contributes less to the dephasing pro-

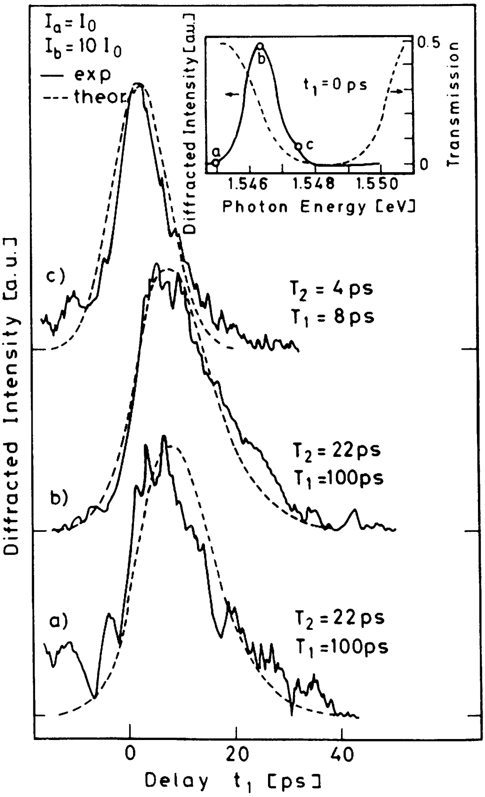

Fig. 6.16. Two-pulse photon echo experiments from two-dimensional excitons in GaAs-AlGaAs quantum wells. Experimental (——) and theoretical (– – –) scattered intensity as a function of the delay time t_1 for three different photon energies. The data show different relaxation times T_2 depending on the spectral position of the excitation pulse within the heavy-hole exciton transition. The insert gives the scattered intensity at zero delay (*solid curve*) together with the transmission spectrum (*dashed curve*) [6.132]

cess. Very recent investigations of high-quality single quantum wells show a homogeneously broadened exciton band. Under these conditions acoustic phonon scattering is found to be the dominant broadening mechanism of the 2*D* excitons [6.148].

6.3.2 Three-Pulse Echos

Experiments with three incident pulses constitute an important extension of the preceding coherent techniques. A schematic of this method was shown in Fig. 6.1c. Adding a third excitation pulse – which enters the sample at a time t_2 after the second pulse – gives new possibilities for studying molecular systems. For a two-level system, the three-pulse technique allows one to determine T_1 in a coherent experiment by varying the delay time t_2. When other molecular levels are involved in the relaxation process, a third pulse at a wavelength differing from that of the first two excitation pulses gives information on the path of the energy decay.

The three-pulse echo is calculated for a two-level system by solving (6.7) for the appropriate pulse sequence. The solution for the polarization $P(t)$ contains a number of different terms, which describe (i) the single-pulse excitation due to pulses a, b, and c, radiating in the directions $\boldsymbol{k}_a$, $\boldsymbol{k}_b$, and $\boldsymbol{k}_c$, respectively, (ii) two-pulse echos originating from pairs of excitation pulses radiating in the direction $2\boldsymbol{k}_i - \boldsymbol{k}_j$ for the various pulses $i, j = a, b, c$, (iii) higher-order terms of the order A^5, and finally (iv) the three-pulse echo:

$$P_{3\mathrm{PE}}(t) \propto \int d\omega\, f(\omega) \exp[-\mathrm{i}\omega(t - t_1) - (t_1 + t)/T_2] G(T_1, t_2) \qquad (6.19)$$

$$\times \sin A_a \sin A_b \sin A_c \exp[-\mathrm{i}(\boldsymbol{k}_b + \boldsymbol{k}_c - \boldsymbol{k}_a)r] \ ,$$

where $G(T_1, t_2)$ depends on the level scheme involved. For a closed system consisting of only two states $|a\rangle$ and $|b\rangle$, $G(T_1, t_2)$ has the form $G^c(T_1, t_2) = \exp(-t_2/T_1)$. For an open system, where the upper level decays to a long-lived ($\tau \gg t_1, t_2, t$) state, which is not probed, $G(T_1, t_2)$ is $G^0(T_1, t_2) = 1 + \exp(-t_2/T_1)$. Equation (6.19) suggests a variety of possibilities for applying the three-pulse echo technique.

1) Variation of the excitation time t_1 allows the determination of the dephasing time T_2 in the case of inhomogeneously and homogeneously broadened transitions (in the same way as in the two-pulse echo experiment).

2) Variation of the time t_2 gives access to the population decay of the upper state. The experimentally observed kinetics depend on the details of the molecular system. If a closed two-level system is investigated, the coherent signal intensity decays with $\exp(-2t_2/T_1)$. A more complex time dependence is observed for an open system where the decay of the signal is proportional to $[1 + \exp(-t_2/T_1)]^2$; i.e. one observes a biexponential decay with decay times $T_1/2$ and T_1, and the signal shows a constant background. The repopulation of the lower level $|b\rangle$ may also be deduced from the later kinetics.

3) The constant background, which is found due to the long-lived intermediate state in open systems allows accumulation of the echo by a sequence of excitation pulse pairs with a repetition rate faster than the spectral cross-correlation time or the repopulation of the ground state. The accumulation of the grating may become so efficient that even weak cw mode-locked lasers can be used to induce a grating and to stimulate an echo.

4) Other aspects of the three-pulse echo technique may be inferred from the grating picture of the three-pulse echo experiment. The first two exciting pulses induce a population grating for the two levels coupled by the two pulses. The populations of the ground and excited state are changed. Energy transfer of either of the two grating states can be monitored. Using the third pulse at a new wavelength, it becomes possible to selectively monitor the relaxation processes. An example of such a two-color echo will be given below.

The laser systems for three-pulse or induced-grating experiments are cw mode-locked dye lasers with a repetition rate of ~100 MHz and a mean power of 30 mW. In some cases, amplified pulses from cw mode-locked dye lasers at repetition rates of 10–100 Hz were applied. For high repetition rate lasers it is advantageous to use perpendicular polarizations for the excitation and probing process in order to remove artifacts due to temperature changes.

a) Measurements of Energy Relaxation Times

A number of interesting grating experiments were performed by *Ippen*'s group using femtosecond light pulses [6.140–142]. In Fig. 6.17 the three-pulse echo experiment was done with amplified 75 ps pulses ($\lambda = 620$ nm) from a colliding pulse mode-locked ring dye laser (repetition rate of the amplified pulses 10 Hz) [6.147]. The first two excitation pulses with wave vectors k_a and k_b entered the sample simultaneously, i.e. $t_1 = 0$. The scattered energy induced by a third pulse is plotted in Fig. 6.17 as a function of the delay time t_2. Two different samples, the dyes cresyl violet and oxazine 720, were investigated and the results are shown in Fig. 6.17a and b, respectively. Both dyes were embedded in a thin film of a polymethylmethacrylate (PMMA) polymer and held at 15 K. The excitation laser pulses populate vibronic levels in S_1, the first excited electronic state of the dyes. The first decay of the signal occurs on a time scale of several 100 fs. It results from an energy redistribution within the electronic state of the dye molecules. Similar rapid relaxation processes were found for dye molecules in solutions at room temperature [6.149]. At later times t_2, longer than 2 ps, a constant level of the signal is approached which decays within nanoseconds with the S_1 lifetime. The different amplitudes of the slower component found for the two dyes suggest complicated relaxation processes. They cannot be explained by simple closed or open two-level systems.

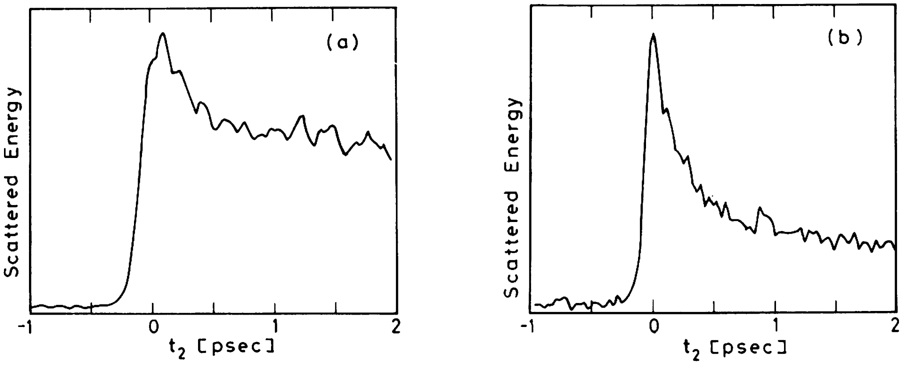

Fig. 6.17. Three-pulse scattering experiment from the organic dye molecules cresyl violet (**a**) and oxazine 720 (**b**) at 15 K using femtosecond light pulses at 620 nm. The scattered energy is plotted as a function of time t_2 for zero relative delay t_1. The signal decay with a time constant of several hundred femtoseconds corresponds to the energy redistribution within the first excited electronic states of the dye molecules [6.142]

b) Measurements of Dephasing Times

Ippen et al. have extended their experiments to measure the short dephasing times in dye molecules. The dephasing processes were determined by varying the time t_1, while keeping t_2 constant at 1.3 ps. The signal scattered by the third pulse was detected in two directions $k_4 = k_c + k_b - k_a$ and $k_5 = k_c + k_a - k_b$. It has been shown in [6.142] that inhomogeneously broadened transitions with long dephasing times $T_2 > t_p$ give scattered signal curves which do not peak at time zero.

Figure 6.18 shows the results for cresylviolet in PMMA at 15 K (Fig. 6.18a) and at 290 K (Fig. 6.18b). The asymmetry is detected for the low-temperature sample. One observes a 60 fs separation of the peaks of the signal curves which demonstrates the presence of inhomogeneous line broadening. With increasing temperature the splitting of the peaks decreases. At room temperature (see Fig. 6.18b) the coincidence of the two signal curves suggests that homogeneous broadening dominates. The same experiments have been performed with Nile blue and oxazine 720. For both dyes the scattered curves coincide over the entire temperature range (15–300 K). These results have been explained as follows: For Nile blue and oxazine 720, the excitation photons at 620 nm have energies of several hundred wavenumbers in excess of the 0–0 transition energy. At large excess energies, background states of high densities exist and a rapid decay of the initially prepared states into these background states can occur. In cresyl violet, on the other hand, low-lying vibronic states, interacting with a small number of background states, were populated; these decay relatively slowly at low temperatures.

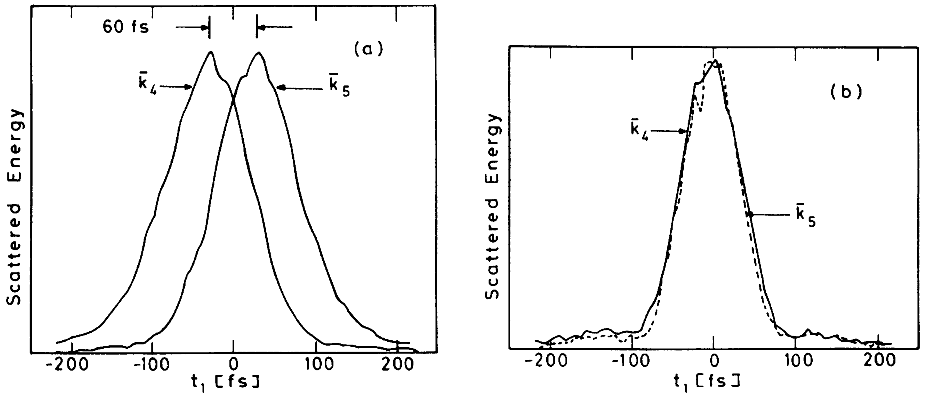

Fig. 6.18a, b. Three-pulse echo experiments for the study of dephasing processes in large dye molecules. For a constant pulse separation, $t_2 = 1.3$ ps, the first delay time t_1 was varied and the three-pulse echo energy was detected in the two directions $k_4 = k_c + k_b - k_a$ and $k_5 = k_c + k_a - k_b$. The asymmetry found in (**a**) – cresyl violet in PMMA at 15 K – indicates the presence of inhomogeneous line broadening. At higher temperatures the asymmetry disappears. At room temperature (**b**) the two curves coincide. Here, homogeneous line broadening is dominant [6.142]

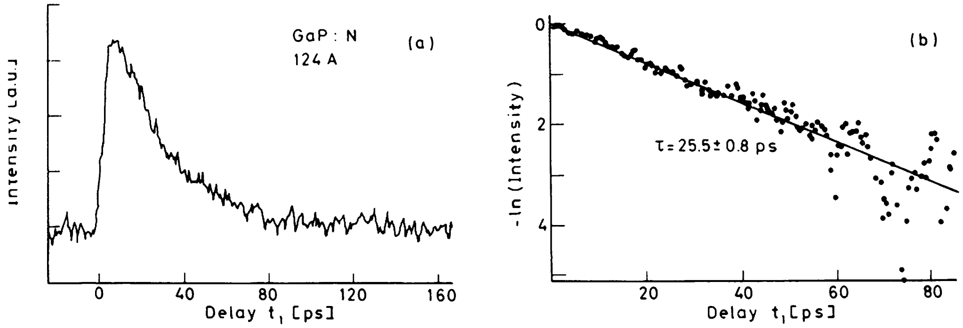

Fig. 6.19a, b. Accumulated photon echo from the nitrogen bond exciton in GaP:N at 1.5 K (λ = 534.95 nm). The echo intensity is plotted in a linear scale (**a**) and in a logarithmic scale (**b**) versus delay time t_1. The low-temperature decay time of 25.5 ps is interpreted as the exciton relaxation time out of the initially excited A state [6.131]

c) Accumulated Three-Pulse Echos

Accumulated three-pulse echos have been observed in a number of molecular crystals and semiconductors where the existence of a long-lived bottleneck state allowed the accumulation of the population grating [6.9,134,136–138]. The experiments discussed here were performed by *Wiersma*'s group [6.131]. The authors investigated nitrogen-doped GaP with a N-concentration of $1.3 \times 10^{16}\,\mathrm{cm}^{-3}$. The nitrogen bound exciton at 534.95 nm was investigated at 1.5 K. In optical absorption only the A-state ($J = 1$) can be reached from the ground state ($J = 0$) while the energetically lower B-state ($J = 2$) is forbidden and is only seen in emission. The long lifetime of 4 µs makes the B-state a bottleneck state. In the experiment a synchronously pumped picosecond dye laser was used at the high repetition rate of 80 MHz without amplification. The time dependence of the accumulated echo intensity as a function of the delay time t_1 is plotted on a linear scale and logarithmic scale in Fig. 6.19a and b, respectively. From Fig. 6.19b, a low-temperature decay time of 25.5 ps was deduced. This decay time is interpreted as the exciton relaxation time from the A- to the B-state. The rapid transfer process explains the absence of the A-line in the low-temperature emission spectrum. The temperature dependence of the decay times gives two activation energies. It appears that two distinct interaction processes determine the exciton lifetime.

d) Two-Color Echos

The three-pulse echo proves to be a versatile tool for the study of vibrational deactivation processes when different laser frequencies are applied for the excitation and probing processes. In the upper part of Fig. 6.20 a four-level system (A) is depicted, where the vibrational states $|a\rangle$ and $|b\rangle$ belong to the electronic

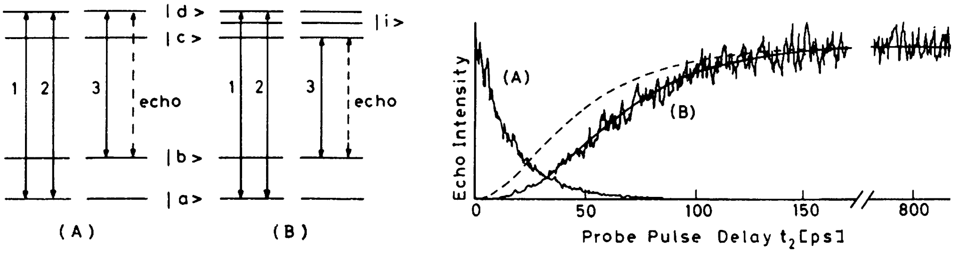

Fig. 6.20. Two-color stimulated photon echos applied to the study of energy relaxation pathways. Left part: Level scheme of the two-color experiment. In case A the first two excitation pulses 1 and 2 generate the population grating in states $|a\rangle$ and $|d\rangle$. Pulses 3 has a wavelength probing only the grating of levels $|b\rangle$ and $|d\rangle$. Varying the delay time t_2 between pulses 2 and 3 allows one to measure the decay of the population of state $|d\rangle$ (curve A). In case B the wavelength of the probing pulse is selected in order to probe states $|b\rangle$ and $|c\rangle$. An echo found with this probing wavelength allows one to follow the population grating of state $|c\rangle$ or $|b\rangle$ built up in the course of relaxation out of state $|d\rangle$. Curve B in the right part of the figure shows a delayed build-up of this echo suggesting the existence of additional levels $|i\rangle$ populated during the relaxation process [6.131]

ground state, and $|c\rangle$ and $|d\rangle$ to the excited electronic state. With two excitation pulses 1 and 2, a population grating is generated in the levels $|a\rangle$ and $|d\rangle$; the probe pulse 3 connects levels $|b\rangle$ and $|d\rangle$. When the inhomogeneous broadening in the different levels is correlated, the third pulse generates an echo signal. The echo amplitude measured as a function of the time t_2 monitors the population decay of state $|d\rangle$. Data from a related experiment are shown in curve A of the right part of Fig. 6.20. The system pentacene in naphthalene was investigated. The first excitation pulse at 17 335 cm^{-1} prepares a vibrational level at 747 cm^{-1} above the absorption origin. The probing pulse at $\nu_3 = 16\,579\,\mathrm{cm}^{-1}$ monitors the occupation of state $|d\rangle$; curve A may be fitted by an exponential decay with a time constant of 33 ps. With the smaller probing frequency $\nu_3/c = 15\,832\,\mathrm{cm}^{-1}$ transitions between levels $|b\rangle$ and $|c\rangle$ are monitored [see Fig. 6.20, scheme (B)]. According to the experimental curve B in the right part of Fig. 6.20 no signal is detected at time zero, i.e. no population is found in the two levels $|b\rangle$ and $|c\rangle$. The echo intensity starts to increase delayed. Within 100 ps it reaches a plateau, where the signal stays constant for the observation time of 800 ps (the lifetime of state $|c\rangle$ is 20 ns). The echo-curve B indicates a population transfer from level $|d\rangle$ to level $|c\rangle$. A more careful inspection of the experimental data suggests a complex transfer process. The experimental echo-curve B deviates from the broken curve which is calculated for a direct population transfer from state $|d\rangle$ to state $|c\rangle$. As a consequence, the authors conclude that there exist intermediate levels $|i\rangle$ with short lifetimes of the order of 20 ps involved in the relaxational processes from level $|d\rangle$ to level $|c\rangle$.

This section clearly demonstrates the power of time-resolved multiple-pulse coherent techniques. The possibility of measuring dephasing times T_2 for inhomogeneously broadened transitions, and also of studying relaxational path ways is very promising. We mention corresponding experiments in the frequency domain: The techniques of spectral hole-burning have become well established. Holes are first "burnt" in an inhomogeneously broadened transition and the widths are subsequently monitored by properly delayed pulses. From the frequency width, the coherent dephasing time may be determined, while the decay of the holes gives information on the energy relaxation T_1 due to cross correlation within the inhomogeneously broadened line or due to the energy decay to other levels. Time- and frequency-domain methods are intimately related. Optimum information is gained by a combination of both techniques.

6.4 Summary

In this chapter we have discussed more than thirty investigations of time-resolved coherent spectroscopy. Many more experiments may be found in the literature. From the various time-resolved coherent techniques we can obtain the following information:

i) whether a transition is homogeneously broadened,
ii) the dephasing time of homogeneously or inhomogeneously broadened transitions,
iii) dominant line broadening mechanisms,
iv) pure dephasing times,
v) energy relaxation times,
vi) mechanisms and pathways of energy relaxation,
vii) collision times,
viii) nonresonant susceptibilities,
ix) transition frequencies within congested spectral regions,
x) precise frequency differences of vibrational modes separated by up to 10 THz.

6.5 Appendix

For the analytical solution of (6.3–5) we introduced in Sect. 6.1.2 the vectorial form $\rho(t)$ of the density matrix and the transformation matrices $\underline{X}(A)$ and $\underline{Y}(t)$ for the excitation process and the free-evolution process, respectively. In detail they are given as follows:

$$\rho_1(t) = \rho_{bb} \; ; \qquad \rho_2(t) = \rho_{ba} \; ; \qquad \rho_3(t) = \rho_{ab} \; ; \qquad \rho_4(t) = \rho_{aa} \tag{6.20}$$

$$Y(t) = \begin{pmatrix} 1 & 0 & 0 & Y_{14} \\ 0 & e^{(i\Delta - 1/T_2)t} & 0 & 0 \\ 0 & 0 & e^{(-i\Delta - 1/T_2)t} & 0 \\ 0 & 0 & 0 & e^{-t/T_1} \end{pmatrix} \tag{6.21}$$

$$X(A_j) = \frac{1}{2} \begin{pmatrix} 1 + \cos A_j & -i \sin A_j e^{ik_j r} & i \sin A_j e^{-ik_j r} & 1 - \cos A_j \\ -i \sin A_j e^{-ik_j r} & 1 + \cos A_j & (1 - \cos A_j) e^{-2ik_j r} & i \sin A_j e^{-ik_j r} \\ i \sin A_j e^{ik_j r} & (1 - \cos A_j) e^{2ik_j r} & 1 + \cos A_j & -i \sin A_j e^{ik_j r} \\ 1 - \cos A_j & i \sin A_j e^{ik_j r} & -i \sin A_j e^{-ik_j r} & 1 + \cos A_j \end{pmatrix} \tag{6.22}$$

where A_j is the pulse area of the excitation pulse, k_j is the wave vector. The matrix element Y_{14} depends on the type of two-level system used. When a closed two-level system is treated, where the system is only in level $|a\rangle$ or $|b\rangle$, Y_{14} becomes $Y_{14} = 1 - \exp(-t/T_1)$. For an open system, where level $|a\rangle$ decays into a long-lived state $|c\rangle$, Y_{14} vanishes: $Y_{14} = 0$.

References

6.1 J.A. Giordmaine, W. Kaiser: Phys. Rev. **144**, 676 (1966)

6.2 S.F. Fischer, A. Laubereau: Chem. Phys. Lett. **35**, 6 (1975)

6.3 D.W. Oxtoby: Adv. Chem. Phys. **40**, 1 (1979)

6.4 R. Kubo: In *Fluctuations, Relaxation and Resonance in Magnetic Systems*, ed. by D. ter Haar (Plenum, New York 1962) p. 101

6.5 R.G. Gordon: Adv. Magn. Reson. **3**, 1 (1968)

6.6 R.G. Gordon: J. Chem. Phys. **39**, 2788 (1963)

6.7 A. Laubereau, W. Kaiser: Rev. Mod. Phys. **50**, 607 (1978)

6.8 A. Penzkofer, A. Laubereau, W. Kaiser: Progr. Quant. Electron. **6**, 55 (1979)

6.9 W.H. Hesselink, D.A. Wiersma: J. Chem. Phys. **73**, 648 (1980)

6.10 A. Yariv: *Quantum Electronics* (Wiley, New York 1975) p. 372

6.11 N.A. Kurnit, I.D. Abella, S.R. Hartmann: Phys. Rev. Lett. **13**, 567 (1964)

6.12 I.D. Abella, N.A. Kurnit, S.R. Hartmann: Phys. Rev. **141**, 391 (1966)

6.13 S.R. Hartmann: IEEE J. Quant. Electron. QE-**4**, 802 (1968)

6.14 R.F. Loring, S. Mukamel: Chem. Phys. Lett. **114**, 426 (1985)

6.15 R.G. Gordon: J. Chem. Phys. **43**, 1307 (1965)

6.16 R.G. Gordon: J. Chem. Phys. **44**, 1830 (1966)

6.17 G. Placzek: *Handbuch der Radiologie*, ed. by E. Marx (Akad. Verlagsges., Leipzig 1934) p. 1

6.18 N. Kohles, A. Laubereau: Appl. Phys. B **39**, 141 (1986)

6.19 B. Dick: Chem. Phys. **113**, 131 (1987)

6.20 N. Bloembergen: Am J. Phys. **35**, 989 (1967)

6.21 W. Kaiser, M. Maier: In *Laser Handbook*, Vol. 2, ed. by F.T. Arecchi, E.O. Schulz-Dubois (North-Holland, Amsterdam 1972) p. 1077

6.22 S.A. Akhmanov: Mater. Res. Bull. **4**, 455 (1969)

6.23 R.L. Carman, F. Shimizu, C.S. Wang, N. Bloembergen: Phys. Rev. A **2**, 60 (1970)

6.24 M. Maier, W. Kaiser, J.A. Giordmaine: Phys. Rev. **177**, 580 (1969)

6.25 Y.R. Shen, N. Bloembergen: Phys. Rev. **137A**, 1786 (1965)
6.26 N. Bloembergen: *Nonlinear Optics* (Benjamin, New York 1965)
6.27 P.D. Maker, R.W. Terhune: Phys. Rev. **137A**, 801 (1965)
6.28 A. Penzkofer, W. Kaiser: Opt. Quant. Electron. **9**, 315 (1977)
6.29 D. von der Linde, A. Laubereau, W. Kaiser: Phys. Rev. Lett. **26**, 954 (1971)
6.30 R.R. Alfano, S.L. Shapiro: Phys. Rev. Lett. **26**, 1247 (1971)
6.31 C.H. Lee, D. Richard: Appl. Phys. Lett. **32**, 168 (1978)
6.32 J.P. Heritage: Appl. Phys. Lett. **34**, 470 (1979)
6.33 J. Kuhl, D. von der Linde: In *Ultrafast Phenomena III*, Proc. Topical Meeting, Garmisch-Partenkirchen, Germany, June 1982, Springer Ser. Chem. Phys., Vol. 23, ed. by K.B. Eisenthal, R.M. Hochstrasser, W. Kaiser (Springer, Berlin, Heidelberg 1982) p. 201
6.34 R. Leonhardt, W. Holzapfel, W. Zinth, W. Kaiser: Chem. Phys. Lett. **133**, 373 (1987)
6.35 A. Laubereau: Chem. Phys. Lett. **27**, 600 (1974)
6.36 A. Laubereau, G. Wochner, W. Kaiser: Opt. Commun. **17**, 91 (1976)
6.37 W. Zinth, H.J. Polland, A. Laubereau, W. Kaiser: Appl. Phys. B **26**, 77 (1981)
6.38 H. Graener, A. Laubereau, J.W. Nibler: Opt. Lett. **9**, 165 (1984)
6.39 M.L. Geirnaert, G.M. Gale, C. Flytzanis: Phys. Rev. Lett. **52**, 815 (1984)
6.40 M.L. Geirnaert, G.M. Gale: Chem. Phys. **86**, 205 (1984)
6.41 J. Chesnoy: Chem. Phys. Lett. **125**, 267 (1986)
6.42 G.M. Gale, P. Guyot-Sionnest, W.Q. Zheng: Opt. Commun. **58**, 395 (1986)
6.43 M. van Exter, A. Lagendijk: Opt. Commun. **56**, 191 (1985)
6.44a W. Zinth, R. Leonhardt, W. Holzapfel, W. Kaiser: J. Quant. Electron. QE-**24**, 455 (1988)
6.44b R. Leonhardt, W. Holzapfel, W. Zinth, W. Kaiser: private communication
6.45 D.W. Oxtoby, D. Levesque, J.J. Weis: J. Chem. Phys. **68**, 5528 (1978)
6.46 J.P. Riehl, D.J. Diestler: J. Chem. Phys. **64**, 2593 (1976)
6.47 D.J. Diestler, R.S. Wilson: J. Chem. Phys. **62**, 1572 (1975)
6.48a P.A. Madden, R.M. Lynden-Bell: Chem. Phys. Lett. **38**, 163 (1976)
6.48b R.M. Lynden-Bell, G.C. Tabisz: Chem. Phys. Lett. **46**, 175 (1977)
6.49 S. Bratos, E. Marechal: Phys. Rev. A **4**, 1078 (1971)
6.50 W.G. Rothschild: J. Chem. Phys. **65**, 455 (1976)
6.51 W.G. Rothschild: J. Chem. Phys. **65**, 2958 (1976)
6.52 D.J. Diestler, J. Manz: Mol. Phys. **33**, 227 (1977)
6.53 R. Wertheimer: Mol. Phys. **35**, 257 (1978)
6.54 R. Wertheimer: Chem. Phys. Lett. **52**, 224 (1977)
6.55 D. Oxtoby: J. Chem. Phys. **70**, 2605 (1979)
6.56 R.M. Shelby, C.B. Harris, P.A. Cornelius: J. Chem. Phys. **70**, 34 (1979)
6.57 S.F. Fischer, A. Laubereau: Chem. Phys. Lett. **55**, 189 (1978)
6.58 S. Mukamel: Phys. Rev. A **26**, 617 (1982)
6.59 S. Mukamel: Phys. Rev. A **28**, 3480 (1983)
6.60 W.G. Rothschild, M. Perrot, F. Guillaume: Chem. Phys. Lett. **128**, 591 (1986)
6.61 W. Zinth, A. Laubereau, W. Kaiser: Opt. Commun. **26**, 457 (1978)
6.62 F.M. Kamga, M.G. Sceats: Opt. Lett. **5**, 126 (1980)
6.63 M.G. Sceats, F. Kamga, D. Podolski: In *Picosecond Phenomena II*, Proc. Topical Meeting, Cape Cod, Mass., USA, June 1980, Springer Ser. Chem. Phys., Vol. 14, ed. by R.M. Hochstrasser, W. Kaiser, C.V. Shank (Springer, Berlin, Heidelberg 1980) p. 348
6.64 W. Zinth: Opt. Commun. **34**, 479 (1980)
6.65 B.K. Rhee, W.E. Bron, J. Kuhl: Phys. Rev. B **30**, 7358 (1984)
6.66 S. Velsko, J. Trout, R.M. Hochstrasser: J. Chem. Phys. **79**, 2114 (1983)
6.67 D.E. McCumber, M.D. Sturge: J. Appl. Phys. **34**, 1682 (1963)
6.68 R. Orbach: IEEE Trans. Sonics Ultrason. **SU14**, 140 (1967)
6.69 R. Orbach, L.A. Vredevoe: Physics **1**, 91 (1964)
6.70 P.G. Klemens: Phys. Rev. **148**, 845 (1966)

6.71 I.I. Abram, R.M. Hochstrasser: J. Chem. Phys. **72**, 3617 (1980)
6.72 S. Velsko, R.M. Hochstrasser: J. Chem. Phys. **82**, 2180 (1985)
6.73 G.J. Small: Chem. Phys. Lett. **57**, 501 (1978)
6.74 K.E. Jones, A.H. Zewail: In *Advances in Laser Chemistry*, ed. by A.H. Zewail (Springer, New York 1978) p. 196
6.75 C.B. Harris, R.M. Shelby, P.A. Cornelius: Phys. Rev. Lett. **38**, 1415 (1977)
6.76 C.B. Harris J. Chem. Phys. **67**, 5607 (1977)
6.77 P. de Bree, D.A. Wiersma: J. Chem. Phys. **70**, 790 (1978)
6.78 R.G. Delle Valle, P.F. Fracassi, R. Righini, S. Califano: Chem. Phys. **74**, 179 (1983)
6.79 D.D. Dlott: Ann. Rev. Phys. Chem. **37**, 157 (1986)
6.80 W.H. Hesselink, D.A. Wiersma: Chem. Phys. Lett. **65**, 300 (1979)
6.81 D. von der Linde, J. Kuhl, H. Klingenberg: Phys. Rev. Lett. **44**, 1505 (1980)
6.82 A. Laubereau, D. von der Linde, W. Kaiser: Phys. Rev. Lett. **27**, 802 (1971)
6.83a W.E. Bron, J. Kuhl, B.K. Rhee: Phys. Rev. B **34**, 6961 (1986)
6.83b J. Kuhl, W.E. Bron: Solid State Commun. **49**, 935 (1984)
6.84 G.M. Gale, A. Laubereau: Opt. Commun. **44**, 273 (1983)
6.85 A. Laubereau, G. Wochner, W. Kaiser: Opt. Commun. **14**, 75 (1975)
6.86 A. Laubereau: In *Semiconductors Probed by Ultrafast Laser Spectroscopy*, Vol. 1, ed. by R.R. Alfano (Academic, Orlando 1984) p. 275
6.87 G.M. Gale, F. Vallee, C. Flytzanis: Phys. Rev. Lett. **57**, 1867 (1986)
6.88 G.M. Gale, P. Guyot-Sionnest, W.Q. Zheng, C. Flytzanis: Phys. Rev. Lett. **54**, 823 (1985)
6.89 G.M. Gale, F. Vallee, C. Flytzanis: In *Time Resolved Vibrational Spectroscopy*, Proc. Conf. June 1985, Springer Proc. Phys. IV, ed. by A. Laubereau, M. Stockburger (Springer, Berlin, Heidelberg 1985) p. 117
6.90 C. Flytzanis, G.M. Gale, M.L. Geirnaert: In *Applications of Picosecond Spectroscopy to Chemistry*, ed. by K.B. Eisenthal (Reidel, Amsterdam 1984) p. 205
6.91 P.L. Decola, R.M. Hochstrasser, H.P. Frommsdorff: Chem. Phys. Lett. **72**, 1 (1980)
6.92 B.H. Hesp. D.A. Wiersma: Chem. Phys. Lett. **75**, 423 (1980)
6.93 K. Duppen, B.H. Hesp, D.A. Wiersma: Chem. Phys. Lett. **79**, 399 (1981)
6.94 K. Duppen, D.P. Weitekamp, D.A. Wiersma: J. Chem. Phys. **79**, 5835 (1983)
6.95 C.L. Schosser, D.D. Dlott: J. Chem. Phys. **80**, 1394 (1984)
6.96 F. Ho, W.S. Tsay, J. Trout, R.M. Hochstrasser: Chem. Phys. Lett. **83**, 5 (1981)
6.97 F. Ho, W.S. Tsay, S. Velsko, R.M. Hochstrasser: Chem. Phys. Lett. **97**, 141 (1983)
6.98 S. Velsko, J. Trout, R.M. Hochstrasser, J. Chem. Phys. **79**, 2114 (1983)
6.99 T.J. Trout, S. Velsko, R. Bozio, P.L. Decola, R.M. Hochstrasser: J. Chem. Phys. **81**, 4746 (1984)
6.100 S. Velsko, R.M. Hochstrasser: J. Chem. Phys. **89**, 2240 (1985)
6.101 R.M. Hochstrasser: In *Time Resolved Vibrational Spectroscopy*, Proc. Conf. June 1985, Springer Proc. Phys. IV, ed. by A. Laubereau, M. Stockburger (Springer, Berlin, Heidelberg 1985) p. 96
6.102 T.J. Kosic, R.E. Cline Jr., D.D. Dlott: J. Chem. Phys. **81**, 4932 (1984)
6.103 R.F. Loring, S. Mukamel: In *Time Resolved Vibrational Spectroscopy*, Proc. Conf. June 1985, Springer Proc. Phys. IV, ed. by A. Laubereau, M. Stockburger (Springer, Berlin, Heidelberg 1985) p. 293
6.104 H.R. Telle, A. Laubereau: Chem. Phys. Lett. **94**, 467 (1983)
6.105 W. Zinth, W. Kaiser: In *Organic Molecular Aggregates*, Springer Ser. Solid-State Sci., Vol. 49, ed. by P. Reinecker, H. Haken, H.C. Wolf (Springer, Berlin, Heidelberg 1983) p. 124
6.106 R. Leonhardt, W. Holzapfel, W. Zinth, W. Kaiser: private communication
6.107a H. Graener, A. Laubereau: Opt. Commun. **54**, 141 (1985)
6.107b H. Graener, A. Laubereau: In *Time Resolved Vibrational Spectroscopy*, Proc. Conf. June 1985, Springer Proc. Phys. IV, ed. by A. Laubereau, M. Stockburger (Springer, Berlin, Heidelberg 1985) p. 11

6.108 S. De Silvestri, J.G. Fujimoto, E.P. Ippen, E.B. Gamble Jr., L.R. Williams, K.A. Nelson: Chem. Phys. Lett. **116**, 146 (1985)
6.109 A. Laubereau, G. Wochner, W. Kaiser: Chem. Phys. **28**, 363 (1978)
6.110 A. Laubereau, G. Wochner, W. Kaiser: Phys. Rev. A **13**, 2212 (1976)
6.111 C.B. Harris, H. Auweter, S.M. George: Phys. Rev. Lett. **44**, 737 (1980)
6.112 S.M. George, H. Auweter, C.B. Harris: J. Chem. Phys. **73**, 5573 (1980)
6.113 S.M. George, C.B. Harris: Phys. Rev. A **28**, 863 (1983)
6.114 S.M. George, A.L. Harris, M. Berg, C.B. Harris: J. Chem. Phys. **80**, 83 (1984)
6.115 J.C. Diels: IEEE J. Quant. Electron. QE-**16**, 1020 (1980)
6.116 R.F. Loring, S. Mukamel: J. Chem. Phys. **83**, 2116 (1985)
6.117 W. Zinth, W. Kaiser: In *Lecture Notes in Physics*, Vol. 182, ed. by J.D. Harvey, D.F. Walls (Springer, New York 1983) p. 152
6.118 W. Zinth, M.C. Nuss, W. Kaiser: Chem. Phys. Lett. **88**, 257 (1982)
6.119 W. Zinth, M.C. Nuss, W. Kaiser: Opt. Commun. **44**, 262 (1983)
6.120 W. Zinth, M.C. Nuss, W. Kaiser: Phys. Rev. A **30**, 1139 (1984)
6.121 M.C. Nuss, W. Zinth, W. Kaiser: J. Opt. Soc. Am. B **2**, 322 (1985)
6.122 M.A. Collins, P.A. Madden, A.D. Buckingham: Chem. Phys. **94**, 291 (1985)
6.123 M.D. Crisp: Phys. Rev. A **1**, 1604 (1970)
6.124 H.J. Hartmann, A. Laubereau: Opt. Commun. **47**, 117 (1983)
6.125 H.J. Hartmann, A. Laubereau: J. Chem. Phys. **80**, 4663 (1984)
6.126 H.J. Hartmann, K. Bratengeier, A. Laubereau: Chem. Phys. Lett. **108**, 555 (1984)
6.127 H.J. Hartmann, H. Schleicher, A. Laubereau: Chem. Phys. Lett. **116**, 392 (1985)
6.128 D.W. Phillion, D.J. Kuizenga, A.E. Siegman: Appl. Phys. Lett. **27**, 85 (1975)
6.129 A.E. Siegman: Appl. Phys. Lett. **30**, 21 (1977)
6.130 R. Trebino, A.E. Siegman: J. Chem. Phys. **79**, 3621 (1983)
6.131 K. Duppen, L.W. Molenkamp, D.A. Wiersma: Physica **127B**, 349 (1984)
6.132 L. Schultheis, M.D. Sturge, J. Hegarty: Appl. Phys. Lett. **47**, 995 (1985)
6.133 W.H. Hesselink, D.A. Wiersma: Chem. Phys. Lett. **56**, 227 (1978)
6.134 W.H. Hesselink, D.A. Wiersma: Phys. Rev. Lett. **43**, 1991 (1979)
6.135 W.H. Hesselink, D.A. Wiersma: J. Chem. Phys. **74**, 886 (1981)
6.136 L.W. Molenkamp, D.A. Wiersma: J. Chem. Phys. **80**, 3054 (1984)
6.137 K. Duppen, D.P. Weitekamp, D.A. Wiersma: Chem. Phys. Lett. **108**, 551 (1984)
6.138 K. Duppen, D.P. Weitekamp, D.A. Wiersma: Chem. Phys. Lett. **106**, 147 (1984)
6.139 L.W. Molenkamp, D.P. Weitekamp, D.A. Wiersma: Chem. Phys. Lett. **99**, 382 (1983)
6.140 A.M. Weiner, E.P. Ippen: Opt. Lett. **9**, 53 (1984)
6.141 S. De Silvestri, A.M. Weiner, J.G. Fujimoto, E.P. Ippen: Chem. Phys. Lett. **112**, 195 (1984)
6.142 A.M. Weiner, S. De Silvestri, E.P. Ippen: J. Opt. Soc. Am. B **2**, 654 (1985)
6.143 J.L. Skinner, H.C. Andersen, M.D. Fayer: J. Chem. Phys. **75**, 3195 (1981)
6.144 W.H. Hesselink, D.A. Wiersma, J. Chem. Phys. **75**, 4192 (1981)
6.145 D.P. Weitekamp, K. Duppen, D.A. Wierma: Phys. Rev. A **27**, 3089 (1983)
6.146 H. Paerschke, K.E. Süsse, B. Wilhelmi: Opt. Quant. Electron. **15**, 41 (1983)
6.147 J.G. Fujimoto, T.K. Yee: Appl. Phys. B **34**, 55 (1984)
6.148 L. Schultheis, A. Honold, J. Kuhl, K. Köhler, C.W. Tu: Phys. Rev. B **34**, 9027 (1986)
6.149 A.M. Weiner, E.P. Ippen: Chem. Phys. Lett. **114**, 456 (1985)

Subject Index

Aberration correction 67
Absorption 314
- grating 66
- saturation 283
- spectra of electron-hole plasmas 131
Accumulated echo 268, 271
Acetone 247
Acetonitrile 247
Acetylene (C_2H_2) 286
Acoustic phonon 86
Acousto-optic mode-locking 14
Active mode-locking 7
Adiabatic photodissociation 338
ADP (ammonium dihydrogen phosphate) 40, 41, 44, 50, 52
Adsorbates 95
Ag (silver) 94, 95
AgBr 91
AgCl 94
$AgGaS_2$ 46
Air/liquid interface 96
Air/solid interface 96
Au (gold) 94
Aluminium 176
Amino acids 254
Amorphization 161
Amplification 19
Angle tuning 47, 52
Anharmonic coupling 292, 311
- intramolecular 290
Anharmonic intramolecular interactions 286
Anharmonic mixing 291
Anharmonicities of potential 286
Anisotropic Raman tensor 243
Anisotropy of Raman polarization 81
Antenna energy transfer 390
Approximate phase-matching 37
Aqueous solution 65
Artificial nonlinearity 92
Association of alcohol molecules 290
Autocorrelation function 89
Autocorrelation measurements 56
Automatic phase-matching 65, 72, 77
7-azaindole dimer 348
Azulene 300

Backward emission 73
Bacterial reaction centers 384
Bacteriorhodopsin 396
Bandwidth product 56
Barium sodium niobate ($Ba_2NaNb_3O_{15}$) 49
Barium vapor 80
Bathorhodopsin 401
Beam divergence 38
Benzene alcohol 97, 253, 258
Benzophenon 330
1.1′-binaphthyl 323
Binary collisions 248
Biradicals 339
Bistability 91
BK-7 glass 91
Bleaching dynamics of organic dyes 314
Bleaching sequence 396
Boltzmann factor 302
Borosilicate glass 69
Bound exciton 93
Bragg scattering 84, 96
Brilliant green 87
Buffer gas 80

Cadmium 62
Cadmium sulfide 91, 93, 116, 134
Calcite 63, 149
Carbenes 333, 334
Carrier thermalization 137
CARS 63, 66, 250
Cascade process 42
CCl_4 249, 257, 260
CDA (CsH_2AsO_4) 41
CdS 91, 93, 116, 134
CdSe 134
Cesium vapor 80
CH_2BrCl 256
CH_3CCl_3 81
CH_3I 82
Charge density probing 219

Charge transfer 329
Charged particle emission 172
Chemical intermediates 329
Chirp 25
Chlorobenzene 66
Cholesteric liquid crystals 61
CO_2 158
Coherence peak 67, 88
Coherence time t_c 89
Coherent anti-Stokes Raman probing 59
Coherent anti-Stokes Raman scattering *see* CARS 63, 66, 250
Coherent artifact 138
Coherent spectroscopy 253
– in solids 251
Collision time 255
Collision-induced transitions 290
Color center laser 22
Composite materials 97
Continuum generation 90, 98
Conversion efficiency 38, 40, 49, 78
Coumarin 96, 294, 298
CPM laser 16, 30
Cresyl violet 269
Cross-correlation curve 285
Crown glass K8 97
Crystal damage 53
CS_2 66, 67, 68 (Fig. 3.12c), 72, 97, 157
CuCl 116
Cyanine dyes 61
Cyclohexane C_6H_{12} 249

D_2 98
D_2O 44, 70, 90
Degenerate four-wave mixing (DFWM) 17, 64, 66, 70, 72, 97
Degenerate parametric amplification 41
Density of states 289, 294
Dephasing in liquids 247
Dephasing time T_2 75, 238
Depopulation lifetimes *see* Energy relaxation time T_1 310, 313
Diamond 149, 252
Dielectric breakdown 54, 62
Difference-frequency generation 45
Difference-frequency resonance 69
Diode laser 24
Distributed feedback laser 23, 88
DODCI 71
Double proton transfer 348
Double resonance of nonlinear susceptibility 74
Down conversion 45, 47, 54, 56

Electric dipole transition 241
Electrical isolation 213
Electrical transmission lines 209
Electron donor-acceptor complexes 332
Electron transfer to quinone 389
Electron-hole scattering 190
Electronic autocorrelation measurement 203
Electro-optic Cherenkov radiation 208
Electro-optic wafer prober 218
Energy decay law 307
Energy dissipation to surroundings 296
Energy equalization 284, 309, 313
Energy exchange 292, 294
Energy relaxation time T_1 236, 238, 268, 269, 306
Energy transfer in chlorophylls 390
Energy transfer law 305
Energy transfer to translation 287
Excess population 281
Excited-state proton transfer 341

Factor group 253
Far infrared 45, 52, 53
– applications 221
– generation 46, 47
Femtosecond continuum 51, 91
Femtosecond dye laser 17
Fermi resonance 158, 290
– mixing 292
Fifth harmonic generation 62
Fifth-order correlation function 65
Flow of vibrational energy 286
Fluorescence 368, 404
– excitation spectrum 299
Fourier-transform Raman spectroscopy 259
Four-photon mixing process 69
Fourth harmonic 43
Four-wave difference frequency 63
Four-wave mixing 64, 68, 83, 90, 98
Four-wave up-conversion 62
Frequency mixing 43
Frequency shift 90
Frozen-wave generator 222
Fuchsin 61
Fused silica 70

GaAs 91, 117, 131, 153, 161, 175, 266
Gain coefficient 75
Gain of electron-hole plasmas 131
Gain factor 47
Gain measurements 314
Gain saturation 76
GaP 150, 251, 252, 271
Gaussian beam 38
Ge (germanium) 87, 94, 161

Germinate reactions with CO_2, NO, and O_2 374
Giant-pulse lasers 10
Green plant reaction centers 395
Group delay 38, 41, 42, 77
Group velocity 116, 117
- dispersion 38

H_2O 90
HCl 263
Halorhodopsin 409
Heat conduction 308
Heat pipe 61, 63, 80
Helical structure 61
Heme proteins 357–380
Hexafluoroisopropanol 61
Higher-order cross correlation 59
Higher-order scattering 86
High-power photoconductors 226
High-speed photodetectors 214
High-speed transistors 215
Homogeneously broadened transition 239, 265
Hot-phonon effects 137
Hybrid mode-locking 18
Hydrogen atom transfer 330
Hydrogen gas 77
Hysteresis 92, 96

I_2 (iodine) 328
Image reconstruction 72
Impulsive stimulated Brillouin scattering 86
Impulsive stimulated scattering 78
Incoherent phonons 152
Indigo 345
Induced absorption spectra 119
Induced birefringence 67
Induced dichroism 314
Induced population grating 68, 83
Infrared bleaching 283
Infrared continuum 55
Infrared spectra 367
InGaAs 136
Inhomogeneous broadening 239, 259
Inhomogeneous line 265
Integrated circuits 217, 218, 219
Integrated photoconductors 220
Intensity-and-phase autocorrelator 57
Intensity autocorrelation function 56, 59
Intensity grating 85
Interaction Hamiltonian 236
Interaction length 37, 38
Interfaces 94
Interferometric autocorrelation 57, 58 (Fig. 3.9a)
Interferometric technique 67
Intermolecular energy transfer 303, 304, 305, 306
Intermolecular proton transfer 342
Intermolecular relaxation of energy 295
Intermolecular vibronic relaxation 315
Internal conversion 281, 300
Internal temperature 299, 300, 301
Intervalley scattering 155
Intramolecular energy transfer 286, 290
Intramolecular proton transfer 343
Inverse gap effect 335
Inversion symmetry 37, 53
Isoenergetic combination modes 302
Isolated binary collisions 308

KB5 (potassium penta borate) 44
KDP (potassium dihydrogen phosphate) 38, 39, 40, 41, 43, 51, 53
KD*P 40, 44
Kerr cell 227
Kerr nonlinearity 26
Kramers model 321
$KTiOPO_4$ (KTP) 40

Langevin equation 322
Langmuir-Blodgett film 95
Laser heating 94
Laser-induced breakdown 54
Laser-induced heating 377
Laser-induced orientational grating 87
Lattice temperature 172
Lattice vibrations 209
Light harvesting 390
Light-induced grating 64
Light-induced phase-shift 68
$LiIO_3$ 40, 41, 44, 45, 46, 51, 53
$LiNbO_3$ 38, 39, 41, 47, 49, 50, 51
Local temperature 309
Luminescence 55

Macroscopic heat conduction 311
Melting 94
Metal colloids 98
Metal vapor 61, 78
Methanol 59, 96
Microcanonical distribution 301
Microwave applications 221
Microwave generation 222
Mid-infrared 52, 53
Millimeter wave applications 221
Model for energy transfer 306
Models for primary processes 399

Mode-locked semiconductor 24
Mode-locking 5
- of color center 22
Molecular beam 324, 349
Molecular crystals 152
Molecular dynamics simulations 372
Molecular thermometer 309
Monolayer 95
Mott transition 135
Multiphonon states 156
Multiphoton processes 404
Multiple excitation processes 264
Multiple quantum well 93
Multiple trapping 144

NaCl 70
Ne (neon) 62
Nearly degenerate four-wave mixing 65, 66, 73
Nitrenes 337
Nitrobenzene 66
Nitrogen 256
Noble gases 61
Non-centrosymmetric crystals 42
Noncritical phase-matching 51
Nondegenerate four-wave mixing 65
Nonexponential dephasing 82
Noninvasive probing 212
Nonlinear Kerr media 90
Nonlinear polarization 37
Nonlinear refraction 96
Nonlinear refractive index 66, 67, 91, 92, 96, 100
Nonlinear Schrödinger equation 99, 100
Nonlinear susceptibility $\chi^{(3)}$ 60, 94
Nonlinear transmission lines 210
Nonlinear wave equation 85, 99
Nonresonant susceptibility $\chi^{(3)}_{\mathrm{NR}}$ 246, 249
NOR gate 93

Off-axis geometry 43, 67
One-photon resonance 69, 70, 72
Optical absorption 401, 404
Optical bistability 92, 96
Optical inhomogeneity 50
Optical Kerr effect 97
Optical parametric amplifier (OPA) 48, 50
Optical parametric oscillator (OPO) 47, 48
Optical phase conjugation 67, 69, 70, 73
Optical phonon lifetimes 149
Optical pulse compression 59
Optical rectification 187, 207, 222
Optical spectra 359
Optical Stark effect 93
Optical surface spectroscopy 95
Optoelectronic devices 185
Optoelectronic measurement systems 211
Organic polymers 72
Orientational Kerr effect 66, 67
Orientational relaxation 141
Oxazine 720 269

Parametric continuum 53
Parametric emission 65
Parametric fluorescence 68
Parametric light gate 54
Parametric oscillation 51, 70, 71
Parametric process 285
Parametric superluminescence 48
Passive mode-locking 9, 11, 15
Pentacene in naphthalene 266
Pentadecanoic acid 96
Peptides 254
Phase conjugation 87
Phase-grating 67
Phase-matching 42, 61, 99, 246
Phase-matching bandwidth $\Delta\nu$ 39, 44
Phase memory 86
Phase mismatch 37
Phase modulation 81, 223
Phase relaxation time T_2 236, 237, 247, 251, 267, 270
Phenol 95
Phonon dynamics 146
Photochemistry 395
Photoconducting antenna 224
Photoconducting electrical pulse generators 200
Photoconducting electronic sampling 202
Photoconducting materials 188
Photoconductive switches 221, 227
Photocycle 397
Photodissociation of I_2 328
Photoelectric emission 217
Photo-emissive sampling 217
Photo-excited carrier distribution 139
Photofragmentation 349
Photoisomerization 320, 325
Photon counting 54
Photon echo 240, 265
Photophysics 375
Photoreduction 330
Photosynthesis 374, 380–395
Phycobilin energy transfer 393
Picosecond continuum 44, 53
Picosecond mass spectrometry 349
Picosecond photoconductors 198
Plasma density 172
Plasma frequency 170

Pockel's cell 227
Polarization 36
– mismatch scheme 43
Polydiacetylene 72, 85, 97
Population lifetime T_1 *see also* Energy relaxation time 75, 279, 285, 288, 289, 290, 291, 295, 296, 306, 311
Population probability of vibrational states 302
Proustite (Ag_3AsS_3) 53
Pulse area 238, 243, 244
Pulse compression 25, 93
Pulse dispersion 210
Pulse shape analysis 56
Pump-probe coupling 88
Pump-probe experiment 88
Pure dephasing time T_2^* 238
Pure dephasing time in solids 252
Purple membrane pigments 404
Pyridine 95, 261

Quantum beats 256
Quantum-confined Stark effect 146
Quantum dots 97
Quantum noise 48, 81
Quantum size effects 98
Quantum wells 266
Quantum-well heterostructures 97
α-quartz 149, 252
Quasi-free electrons 54
Quasi-thermal distribution 299
Quasi-thermal equilibrium 313

Radiation damage 192
Radiationless transition 279
Radio frequency mixer 186, 223
Raman echos 83
Raman fiber soliton laser 101
Raman gain 76, 98
Raman-induced Kerr effect 68
Raman spectra 364, 379, 398, 404, 406
Raman-type transitions 69, 242
Rayleigh-type mixing 87
Rb vapor 56
Recombination of I_2 328
Recombination lifetime 146
Redistribution time 295
Regenerative pulsation 92
Relaxation process 55
Relaxation in solids 254
Relaxation of vibronic levels 314
Renormalization of band gap 131
Resonance enhancement 61
Resonance of nonlinear susceptibility 64
Resonant pulse propagation 262
Rhodamine 6G 55, 72, 95
Rhodopsin 396
Ruby 72

Sampling gate 186
Saturation of absorption 138
Saturation intensity 283
Screening by free carriers and excitons 127
Screening of Fröhlich interaction 137
Second harmonic 96
– generation 36, 98–99
– probing 53
– pulse shape 39
Second-order susceptibility 36
Self-diffraction 86, 89
Self-phase modulation 49, 82, 90, 91
SEPI (short excitation and prolonged interrogation spectroscopy) 260
SF_6 77
Signal and idler 47
Silica glass fiber 99
Silicon (Si) 87, 161
Silicon-on-sapphire 173
Silver (Ag) 94, 95
Silver thiagollate ($AgGaS_2$) 46
Single-photon resonance 68
Single-shot autocorrelation technique 58
Single-shot pulse analysis 73
Single-shot technique 57, 60
Singlet oxygen 338
Small-area pulse propagation 83
Small molecular limit 289
Smoluchowski limit 322
Sodium vapor 62
Solitons 99, 100
Solvent effects 319
Solvent polarity 327
Specific heat of molecule 298
State-selective chemistry 279
Stilbene 324, 325, 327
Stimulated amplification 47, 68, 73, 78
Stimulated anti-Stokes Raman scattering 74
Stimulated Brillouin scattering 78
Stimulated electronic Raman scattering 80
Stimulated four-photon generation 70
Stimulated four-wave parametric amplification 99
Stimulated four-wave parametric emission 69
Stimulated parametric devices 44
Stimulated parametric emission 47
Stimulated parametric generator 96
Stimulated Raman amplifier 77

Stimulated Raman excitation 280
Stimulated Raman generator 77
Stimulated Raman interaction 101
Stimulated Raman oscillator 77
Stimulated Raman scattering 59, 73, 98, 244
Stokes-anti-Stokes coupling 74
Stokes pulse 77
Streak camera 14, 228
Subharmonic generation 92
Sum-frequency generation 40, 42, 54, 56, 60
Sum-frequency spectrum 96
Superbroadening 90
Supercontinuum 91
Supercooling 161
Superheating of solid 176
Surface melting 164
Surface polariton 95
Surface second harmonic generation 94, 168
Switching 185
Synchronous mode-locking 13
Synchronous pumping 8

T_1 *see* Energy relaxation time
T_2 *see* Phase relaxation time
Tellurium (Te) 54
Temperature tuning 49
Thermal model 160
Thermal population 301
Thermodynamic equilibrium 301
Third harmonic 52, 63
- generation 43, 60, 94
Third-order autocorrelation 61
Third-order nonlinear susceptibility $\chi^{(3)}$ 36, 60, 97
Three-beam grating technique 88
Three-dimensional phase-matching 84, 89
Three-pulse echo 267
Time-correlated transmission measurements 138
Time-domain metrology 213
Time-of-flight method 175
Time-resolved CARS 76
Time-resolved photoluminescence 133
Time-resolved reflectivity measurements 164
Toluene 258
Transient absorption 297
Transient amplification 75
Transient fluorescence excitation 298
Transient frequency-domain experiments 259
Transient grating 265
Transient hot band 298
Transient hot molecule 301
Transient internal temperature 298
Transient refractive index 67
Transient vibrational distribution of energy 297
Traveling-wave excitation 23
Traveling-wave Pockel's cell 227
Trigger jitter 212
Tuning range 44, 52
Twisted internal charge transfer 326
Two-beam grating 86
Two-color echo 271
Two-dimensional carrier confinement 144
Two-level molecules 84
Two-level system 85
Two-photon absorption 41, 54
Two-photon fluorescence 57
Two-photon resonance 70
Two-photon transition 305
Two-pulse echo 265
Two-pulse fluorescence 282
Two-pulse infrared spectrum 299
Two-step process 305

Ultrafast chemical reactions 319
Ultrafast phase transformations 159
"Umklapp" third-harmonic generation 61
Up-conversion 44, 54, 56, 59, 63, 95
UV pulses 42

Vacuum ultraviolet 62
Velocity overshoot 191
Vibrational dephasing time T_2 279
Vibrational distribution 297
Vibrational excitation 280
Vibrational heating by electronic excitation 300
Vibrational redistribution 279, 294, 297, 299
- in azulene 300
Vibrational relaxation 314
Vibrational-resonant sum-frequency generation 95
Vibrational states 301
Vibrational temperature 296
Visual pigments 401
VT-processes 311
VV-transfer 311

Walk-off angle 38
Water 65, 69
Wave vector mismatch 61

Zero-point fluctuation 68, 78
ZnSe 91, 116, 252